

The carbon sink in China as seen from GOSAT with a regional inversion system based on CMAQ and EnKS

Xingxia Kou¹, Zhen Peng^{2*}, Meigen Zhang^{3,4}, Fei Hu^{3,4}, Xiao Han^{3,4}, Ziming Li⁵, Lili Lei^{2,6}

5 ¹Institute of Urban Meteorology, China Meteorological Administration, Beijing, China

²School of Atmospheric Sciences, Nanjing University, Nanjing, China

³State Key Laboratory of Atmospheric Boundary Layer Physics and Atmospheric Chemistry, Institute of Atmospheric Physics, Chinese Academy of Sciences, Beijing, China

⁴University of Chinese Academy of Sciences, Beijing, China

10 ⁵Beijing Meteorological Observatory, Beijing, China

⁶Key Laboratory of Mesoscale Severe Weather, Ministry of Education, Nanjing University, Nanjing, China

Correspondence to: Z. Peng, pengzhen@nju.edu.cn

Abstract. Top-down inversions of China's terrestrial carbon sink are known to be uncertain because of errors related to the relatively coarse resolution of global transport models and the sparseness of *in situ* observations. Taking advantage of regional chemistry transport models for mesoscale simulation and spaceborne sensors for spatial coverage, the Greenhouse Gases Observing Satellite (GOSAT) column-mean dry mole fraction of carbon dioxide (XCO₂) retrievals were introduced in the Models-3 Community Multi-scale Air Quality (CMAQ) and Ensemble Kalman smoother (EnKS)-based regional inversion system to constrain China's biosphere sink at a spatiotemporal resolution of 64 km and 1 h. In general, the annual, monthly and daily variation in biosphere flux was reliably delivered, attributable to the novel flux forecast model, reasonable CMAQ background simulation, well-designed observational operator, and joint data assimilation scheme (JDAS) of CO₂ concentrations and natural fluxes. The size of the assimilated biosphere sink in China was $-0.47 \text{ PgC yr}^{-1}$, which was comparable with most global estimates (i.e., -0.27 to $-0.68 \text{ PgC yr}^{-1}$). Furthermore, the seasonal patterns were recalibrated well, with a growing season that shifted earlier in the year over central and south China. Moreover, the provincial-scale biosphere flux was re-estimated, and the difference between the *a posteriori* and *a priori* flux ranged from $-7.03 \text{ TgC yr}^{-1}$ in Heilongjiang to 2.95 TgC yr^{-1} in Shandong. Additionally, better performance of the *a posteriori* flux in contrast to the *a priori* flux was statistical detectable when the simulation was fitted to independent observations, indicating sufficient to robustly constrained state variables and

15
20
25
30

improved fluxes estimation. This study serves as a basis for future fine-scale top-down carbon assimilation.

1 Introduction

In the context of human-induced climate change, the Paris Agreement charts the course for the world to transition to a green way of development and outlines the minimum steps to be taken to protect the Earth, which requires all countries to make significant commitments to stabilize atmospheric greenhouse gas concentrations and keep the global average temperature to well under a 2°C rise (UNFCCC 2015). Therewith, a growing number of countries and regions are pledging to achieve net-zero emissions in the second half of this century; for instance, Austria by 2040, Sweden by 2045, the European Union by 2050, and China by 2060. Hence, there has been an increasing demand from policymakers and the scientific community in general for accurate knowledge of CO₂ emissions from anthropogenic sources (so that the targeted reductions are effective) and from biospheric uptake (so that natural reservoirs remain stable) (Ciais et al., 2015; Pinty et al., 2017; Friedlingstein, et al., 2020; Deng et al., 2022). In 2019, the Intergovernmental Panel on Climate Change (IPCC) published a refined methodology report as an update to its 2006 guidelines with the aim to complement them with a bottom-up, transparent framework and highlight the Monitoring and Verification Support (MVS) capacity using independent atmospheric measurements (IPCC, 2019). A great deal of effort has been devoted in recent decades to developing and applying atmospheric CO₂ inversions to constrain global- and regional-scale CO₂ fluxes (Enting et al., 1995; Thompson and Stohl, 2014; Broquet et al., 2011, Peters, et a., 2007; Tian et al., 2014; Kou et al., 2017; Kountouris et al., 2018). Most of these inversions are informed by ground-based observations and global chemistry transport models (CTMs), which is far from sufficient to support the abovementioned needs. Despite the development of surface observation networks with highly accurate continuous data, such as ICOS (the Integrated Carbon Observation System) in Europe, the global distribution of ground-based CO₂ measurements remains rather sparse and inhomogeneous. Consequently, the errors introduced by the incomplete observation network, the uncertainties of the CTMs, as well as inversion framework have been proven to disadvantage in delivering consistent regional flux estimates obtained using state-of-the-art global inversions from the national up to the continental scales (Monteil et al., 2020; Piao et al., 2022; Schuh et al., 2022).

60 Spaceborne sensors, designed specifically to retrieve atmospheric concentrations with unprecedented spatial coverage, have in recent years begun to improve the current understanding of greenhouse gases and the associated CO₂ emissions' MVS capacity. At present, there are several operational CO₂ observation satellites in orbit, including Japan's Greenhouse Gases Observing Satellite (GOSAT; Kuze et al., 2009), GOSAT-2 (Glumb et al., 2014), the US Orbiting Carbon Observatory 2 (OCO-2, Eldering et al., 2017a, 2017b), OCO-3 (Eldering et al., 2019), and China's TanSat (Liu et al., 2018; Yang et al., 65 2018). It is recognized that satellite retrievals of shortwave infrared radiation, despite their uncertainty, are sufficient to reliably capture the seasonal variability of XCO₂ (column-mean dry mole fraction of carbon dioxide), as a first-order question in constraining inversion models (Lindqvist et al., 2015; Li et al., 2017). Furthermore, several centers and universities routinely assimilate GOSAT XCO₂ data into 70 models to estimate terrestrial ecosystem carbon exchange, including Japan's National Institute for Environment Studies (NIES), the United States' National Aeronautics and Space Administration (NASA), France's Laboratoire des Sciences du Climat et de l'Environnement, the Netherland's Institute for Space Research, the UK's University of Edinburgh, Canada's University of Toronto, and China's Nanjing University. As an example, the NIES GOSAT Project provides a Level 4 CO₂ data product, and the 75 monthly regional CO₂ flux estimates for the period 2009–2013, based on XCO₂ retrievals and NIES' global atmospheric tracer transport model with Bayes' theorem, are publicly available (Maksyutov et al., 2013; Takagi et al., 2014). Moreover, NASA's Carbon Flux Monitoring System is another recent top-down global inversion system configured with 4DVar and GEOS-Chem (Goddard Earth Observing System with Chemistry) and concurrently assimilates XCO₂ from GOSAT and OCO-2. It has released 80 the longest available terrestrial flux estimates (from 2010–2018) on self-consistent global and regional scales and has planned future updates of the dataset on an annual basis (Liu et al., 2021). In addition, the University of Edinburgh has simultaneously produced a five-year CH₄ and CO₂ flux estimate for 2010–2014 directly from GOSAT retrievals of XCH₄:XCO₂ by using GEOS-Chem and an ensemble Kalman filter (EnKF) (Feng et al., 2017). Moreover, the Global Carbon Assimilation System has been upgraded 85 by Nanjing University to assimilate the GOSAT XCO₂ retrievals from 2010–2015 with the Ensemble Square Root Filter (EnSRF) algorithm and the Model for Ozone and Related Chemical Tracers version 4 (Jiang et al., 2021; 2022). Overall, the top-down CO₂ biosphere flux datasets inverted from satellite data suggest an improved flux estimation compared with the large uncertainties in process-based

terrestrial biosphere model estimates (Byrne et al., 2019; Chevallier et al., 2019; Chen et al., 2021). Deng
90 et al. (2016) and Wang et al. (2018) further highlighted the importance of improved observational
coverage to better quantify the latitudinal distribution of terrestrial fluxes by combining GOSAT
observations over land and ocean. Also, the sensitivity of observations from GOSAT and OCO-2 to
optimized CO₂ fluxes has been examined using GEOS-Chem, indicating that GOSAT offers greater
sensitivity in Northern Hemisphere spring and summer (Byrne et al., 2017; Wang et al., 2019).

95

Nevertheless, the inversions primarily involved uncertainties in global CTMs, satellite retrievals, *a priori*
fluxes, and inversion frameworks. A GOSAT CO₂ global inversion intercomparison experiment involving
eight research groups found that, as expected, the most robust flux estimates were obtained at large scales
and quickly diverged at subcontinental scales (Chevallier et al., 2015; Houweling et al., 2015; Fu et al.,
100 2021). Generally, the assimilated CO₂ flux (i.e., the analytical field) is a weighted average of background
information and observations, which depends on the correlation coefficient between simulated
concentrations of the observation and the state variable (i.e., CO₂ flux). In particular, considering the
transport errors introduced by global CTMs, the reliability of the regional fluxes inferred from GOSAT
retrievals remains a topic of ongoing discussion (Reuter, et al., 2017; He et al., 2022). Consequently, if
105 we can configure a reasonable simulation of the background CO₂ concentration compared with the coarse
spatiotemporal resolution of the global scale, then the flux constrained by observations can be estimated
more precisely at national and city scales. The step up in inversion resolution and accuracy calls for new
developments in shifting from global to regional inversions.

110 The use of regional CTMs in CO₂ research is more recent. For instance, Huang et al. (2014) demonstrated
the importance of regional CTM performance to assimilation and suggested it is possible to improve the
CO₂ concentration accuracy of the synoptic-scale variation by utilizing EnKF and CMAQ (Multi-scale
Air Quality Modeling System). Zhang et al. (2021) assimilated OCO-2 retrievals with WRF-
Chem/DART (Weather Research and Forecasting model coupled with Chemistry/Data Assimilation
115 Research Testbed) to improve the estimation of CO₂ concentrations. In recent years, several studies have
relied on regional CTMs in CO₂ flux inversions inferred from surface stations, towers, and aircraft flights,
including CMAQ, WRF-Chem, CHIMERE, and the FLEXPART Lagrangian model. Not only terrestrial
ecosystem exchange (e.g. Europe, North America, East Asia) but also urban CO₂ emissions (e.g., Los

Angeles, Paris, Indianapolis) has been estimated, and the importance of regional CTM is increasingly
120 recognized with their advantages in resolving fine-scale CO₂ concentrations (Brioude et al., 2013; Staufer
et al 2016; Lauvaux et al 2016; Thompson et al., 2016; Kou et al., 2017; Zheng et al., 2018; Monteil et
al., 2021). Moreover, the potential use of regional CTM in CO₂ inversions with satellite has been explored
with artificial retrievals by observing system simulation experiments (Peng et al. 2015). Pillai et al. (2016)
125 further concluded that satellite missions such as CarbonSat (Carbon Monitoring Satellite) have high
potential to obtain high-resolution CO₂ fluxes in Germany. However, regional CTMs are rarely used in
satellite carbon data inversion in estimating China's terrestrial carbon sink, even though multimodel
comparisons have reported large uncertainties introduced by global CTMs in China's top-down inversion
(Wang et al., 2021; Piao et al., 2022; Schuh et al., 2022; Wang et al., 2022).

130 Previous studies have highlighted that the simultaneous assimilation of concentrations and fluxes as state
variables can help reduce the uncertainty of both the initial CO₂ fields and the fluxes (Tian et al., 2014;
Peng et al., 2015; Kou et al., 2017). Recently, Peng et al. (2017, 2018, 2020) improved air quality
forecasts and emission estimates over China by developing a novel flux forecast model with the
ensemble-based Joint Data Assimilation Framework (JDAS), so that the extended model can construct
135 ensembles of both concentration and flux at the hourly scale. As an extension to this work, JDAS was
further developed towards a high-resolution inversion of CO₂ fluxes based on CMAQ and Ensemble
Kalman smoother (EnKS) with historical GOSAT observations over China, which holds an advantage
over global models in terms of the CO₂ background information and inversion scheme. To the best of our
knowledge, this is the most up to date estimates of China's biosphere flux informed by a regional CTM
140 and satellite observations. It should prove to be of considerable value, particularly under the framework
of the Paris Agreement, which requires high spatiotemporal resolution inversions of CO₂ flux for carbon
accounting at national scales.

In this paper, we focus on the development of top-down estimates constrained by GOSAT retrievals and
145 CMAQ. Using this unique regional inversion technique, we address the following questions:

1. On what scales can regional CTMs and GOSAT observations facilitate the inversion of China's carbon sink?

2. What is the difference between posterior flux inferred from spaceborne retrievals and prior flux?

150 **2 Methods and Data**

2.1 CMAQ regional transport model

The atmospheric transport and the signature of sources and sinks in CO₂ concentrations were simulated using a regional CTM, i.e., CMAQ, which was originally developed by the US Environmental Protection Agency to model multiple air quality issues over a variety of scales, and has been updated for passive tracers, as in Kou et al. (2013) with a 1–64 km horizontal resolution capability. The CMAQ regional modeling system has already been used in several regional studies and has shown promising performance in capturing the fine-scale spatiotemporal variability of CO₂ mixing ratios (e.g., Kou et al., 2013; 2015; Liu et al., 2013; Huang et al., 2014; Li et al., 2017). The CMAQ configuration used here was a domain of 6720 km × 5504 km with 64 × 64 km² fixed grid cells centered at 35°N and 116°E in a rotated polar stereographic map projection. This domain, having 105 (west–east) × 86 (south–north) grid points, covered the whole of mainland China and its surrounding regions (Fig. 2). The model has 15 vertical layers unequally spaced from the ground to approximately 23 km, half of which are concentrated in the lowest 2 km to improve the simulation of the atmospheric boundary layer.

165 In this study, the initial fields and boundary conditions of atmospheric CO₂ volume fraction were obtained by interpolation of NOAA’s CT2019B, which is a widely recognized estimate of the global distribution of atmospheric CO₂. CT2019B CO₂ concentration were created using the optimized surface fluxes, with a spatial resolution of 3° × 2°, 25 vertical levels, and a temporal resolution of 3 h (Jacobson et al., 2020). In addition, the *a priori* biosphere and ocean fluxes used for simulations within the CMAQ domain were also derived from the CT2019B optimized fluxes at a 3-h intervals, but with a spatial resolution of 1° × 170 1°. The anthropogenic CO₂ emission fluxes were based on the Multi-resolution Emissions Inventory for China, version 1.3, and the Regional Emissions Inventory in Asia, version 3.2, with monthly gridded data at a resolution of 0.25° × 0.25° (Zheng et al., 2018; Kurokawa et al., 2020). The Global Fire Emissions Database, version 4.1s, with monthly gridded data at a resolution of 0.25° × 0.25°, was applied to provide 175 the biomass burning emissions (van der Werf et al., 2017). The abovementioned four individual CO₂ fluxes (i.e., biosphere, fossil fuels, fire, and ocean) were spatially interpolated to the CMAQ grid,

conserving the total mass of emissions. CMAQ integrated and generated a 3D CO₂ concentration ensemble derived by the N ensemble fluxes with perturbed CO₂ initial and boundary conditions. The time step of the CMAQ output is 1 h.

180

In addition, RAMS (Regional Atmospheric Modeling System) provides the three-dimensional meteorological fields, with the lowest seven layers being the same as those in CMAQ. The initial and lateral boundary meteorological fields, sea surface temperatures, and initial soil conditions were prescribed by European Centre for Medium-Range Weather Forecasts reanalysis data with a spatial resolution of $1^\circ \times 1^\circ$ and 6-hourly temporal intervals (Zhang et al., 2002).

185

2.2 JDAS CO₂ assimilation framework

In the joint assimilation framework, besides the application of CMAQ to generate ensemble CO₂ concentrations, a flux forecast model was also designed to represents natural flux variations on account of fluxes acting as model forcing. The EnKS was further designed to joint assimilate CO₂ concentrations and fluxes. A brief description of the flux forecast model as well as the ensemble assimilation scheme is presented below.

190

2.2.1 Flux forecast model

CO₂ flux was treated as the model input, with the result that ensemble samples of fluxes could not be prepared by the CMAQ's forward forecasting. Consequently, a novel flux forecast model was designed to generate the background CO₂ flux ensembles $\mathbf{E}_{i,t+1}^f$, where $i = 1, \dots, N$ refers to the i th ensemble member at time t (Equation 1). The superscripts a, f and p denote “assimilation”, “forecast” and “*a priori*”, respectively.

195

$$\begin{aligned} \mathbf{E}_{i,t+1}^f &= \mathbf{E}_{i,t+1}^p + \left(\overline{\mathbf{E}_{t+1}^f} - \mathbf{E}_{t+1}^p \right) \\ &= \beta \left(\frac{\mathbf{C}_{i,t+1}^f}{\mathbf{C}_{t+1}^f} - \overline{\boldsymbol{\kappa}_t} \right) \mathbf{E}_{t+1}^p + \frac{1}{M} \left(\sum_{j=M-1}^1 \overline{\mathbf{E}_{t-24 \times j}^a} + \mathbf{E}_{t+1}^p \right). \end{aligned} \quad (1)$$

200

First, the *a priori* flux ensemble $\mathbf{E}_{i,t+1}^p$ is created by using the ensemble CMAQ forecast CO₂

concentration $C_{i,t}^f$ forced by the $E_{i,t}^f$, where $\overline{C}_t^f = \frac{1}{N} \sum_{i=1}^N C_{i,t}^f$ stands for the ensemble mean of

$C_{i,t}^f$ and E_{t+1}^p refers to the *a priori* flux. The covariance inflation factor β is further used to keep the ensemble spread of the CO₂ concentration scaling factor $\kappa_{i,t}$. The ensemble mean of $\kappa_{i,t}$ can be

205 expressed as $\overline{\kappa}_t = \frac{1}{N} \sum_{i=1}^N C_{i,t}^f / \overline{C}_t^f = 1$. Next, in the second part of Equation 1, the ensemble mean

of $\overline{E}_{t+1}^f = \frac{1}{M} \left(\sum_{j=M-1}^1 \overline{E}_{t-24 \times j}^a + E_{t+1}^p \right)$ is determined by the assimilated CO₂ flux at the same time

on each day from the previous assimilation cycles among these $M-1$ days (i.e., $\overline{E}_{t-24 \times (M-1)}^a$,

$\overline{E}_{t-24 \times (M-2)}^a$, ..., and $\overline{E}_{t-24 \times 1}^a$, $j = M-1, M-2, \dots, 1$) and the *a priori* CO₂ flux E_{t+1}^p . M refers to

the length of the smoothing window, which was chosen as 4 days.

210

This design follows Peters et al. (2007), in which the useful observational information from the previous assimilation cycle was made beneficial to the next assimilation cycle via a smoothing operator but was further modified to cooperate with the diurnal variation in CO₂ biosphere flux. Then, \overline{E}_{t+1}^f was used to

recenter \overline{E}_{t+1}^p . In contrast to previous flux models without diurnal variation, this new flux model is

215

advantageous insofar as it facilitates the development of assimilation between regional CTM forecasts and observations at the hourly scale, so as to achieve high-resolution inversion. On the other hand, negative flux in carbon assimilation is realistic and reasonable, which are not excluded. In this way, Gaussian assumption is satisfied in JDAS carbon assimilation.

220 2.2.2 EnKS assimilation scheme

The regional assimilation system used in this study, JDAS, was developed based on EnSRF originated from NOAA's operational EnKF system (https://dtcenter.ucar.edu/com-GSI/users/docs/users_guide/GSIUserGuide_v3.7.pdf). The EnSRF algorithm has been modified with the EnKS feature and further extended to simultaneously assimilate multiple chemical initial conditions and 225 emissions with the *in situ* measurements of their atmospheric observations (Peng et al. 2017, 2018, 2020;

Kou et al., 2021).

In the present study, the GOSAT observations were introduced in the EnKS-based JDAS framework to constrain China's biosphere sink, CO₂ concentrations and natural fluxes were designed to be concurrently
 230 assimilated. Hence, both the CO₂ concentrations (\mathbf{C}) and natural fluxes (\mathbf{E}) were regarded as state variables (i.e., $\mathbf{x} = [\mathbf{C}, \mathbf{E}]^T$), and helpful observational information employed in the current assimilation cycle could be efficiently capitalized upon in the next assimilation cycle with reduced uncertainty in the initial CO₂ conditions. Accordingly, the background of the state variables, $\mathbf{x}^f = [\mathbf{C}^f, \mathbf{E}^f]^T$, can be prepared by CMAQ and flux forecast model.

235

Observation operator has been designed to convert the background forecast to observation space. To obtain the simulated observations $H(\mathbf{C}^f)$, observation operator H performs the necessary interpolation from CMAQ forecasts to observation space XCO₂. The simulated CO₂ concentration profiles were mapped into the GOSAT satellite retrieval levels and then vertically integrated based on
 240 the satellite averaging kernel according to the following equation:

$$XCO_2^f = XCO_2^p + \sum_{k=1}^{N_{lev}} \left\{ \left[(y_k^f - y_k^p) \mathbf{A}_k \right] \mathbf{h}_k (I - \mathbf{w})^{-1} \right\} \quad (2)$$

where the subscript k represents the retrieval level, XCO_2^p denotes the *a priori* XCO₂ for retrieval, y_k^p is the *a priori* CO₂ profile for retrieval, \mathbf{A}_k stands for the satellite column-averaged kernel, \mathbf{h}_k is a pressure weighting function, and y_k^f denotes the CMAQ-simulated CO₂ profile interpolated into
 245 the corresponding retrieval levels. As in Equation 1, the superscripts f and p also refer to “forecast” and “*a priori*” in Equation 2. Moreover, \mathbf{w} denotes the RAMS water mole fraction, which was used to map from the CO₂ concentrations to the dry mole fraction, as suggested by Feng et al. (2009). In addition, for the $H(\mathbf{E}^f)$, it should be noted that H includes not only interpolation (i.e. Equation 2) but also CMAQ to convert from flux to simulated XCO₂.

250

The observation-minus-background, OMB, (i.e., $y - H(\mathbf{C}^f)$) is denoted as “observational increments”

or “innovations”, where y refers to GOSAT XCO₂. The analysis \mathbf{x}^a is obtained by adding the innovations to the model forecast with weights K (i.e. Kalman gain matrix), that are determined based on the estimated statistical error covariance of the forecast and the observations based on Equation 3.

$$255 \quad \mathbf{x}^a = \mathbf{x}^f + K(y - H(\mathbf{x}^f)) \quad (3)$$

Consequently, after completing the “forecast step”, K is obtained by minimizing the analysis error covariance with evolved forecast error covariance over time. Then, the associated analyzed state variables, $\mathbf{x}^a = [\mathbf{C}^a, \mathbf{E}^a]^T$, can be updated by applying the EnKS constrained by GOSAT retrievals

in the “analysis step”. Hereafter, AN denotes the analysis fields \mathbf{x}^a and BG denotes the model’s first

260 guess background fields \mathbf{x}^f .

The basic configuration of the JDAS CO₂ inversion settings followed previous studies. For instance, the ensemble size N was set to 50 to sustain the balance between computational cost and ensemble performance. The horizontal covariance localization radius was chosen as 1280 km to localize the observation’s impact and ameliorate the spurious long-range correlations between state variables and observations caused by the limited number of ensemble members (Peng et al., 2023; Houtekamer & Mitchell, 2001; Gaspari & Cohn, 1999). Moreover, the covariance inflation factor β was set to 80 to preserve the ensemble spread. In this study, the assimilation window of EnKS was set to 24 h, and hour-by-hour assimilation was adopted in the novel flux forecast model and fine-scale CMAQ background simulation. In an assimilation cycle, the fluxes for the 24-h smoothing window have been designed to be optimized hour by hour successively. The distribution of ensemble spread of CO₂ flux in January 2016 is provided in Fig. 1. It shows that the values of the ensemble spread ranges from 0.2 to 0.8 in most areas, which are consistent with our previous studies (Peng et al., 2015 in Figure 11c and Peng et al., 2023).

2.3 GOSAT XCO₂ retrievals

275 GOSAT, launched by the Japan Aerospace Exploration Agency in January 2009, was designed to make near-global greenhouse gas measurements in a sun-synchronous orbit. It covers the whole globe in 3 d and has a sounding footprint of approximately 10.5 km. In this study, we assimilated GOSAT XCO₂ retrievals from NASA’s Atmospheric CO₂ Observations from Space Level 2 standard data products

(version ACOS_L2_Lite_FP.9r; data available at
280 https://oco2.gesdisc.eosdis.nasa.gov/data/GOSAT_TANSO_Level2/). This version of processing
supports both nadir and glint soundings. In the case of soundings over water, a check was made to ensure
the observation was made in glint mode. The XCO₂ data from Lite products were bias-corrected (Wunch
et al. 2017; O’Dell et al. 2018). Typically, Level 2 Lite products contain 10–200 useful soundings per
orbit, noting that more than 50% of the spectral data were not processed during retrieval because they
285 did not pass the first cloud screening pre-processing step.

The update for CO₂ flux is given by the observation innovation and the correlations between CO₂
concentrations and emissions, while the correlations are naturally provided by the physics- and
dynamics-based numerical model. Although there are limited observation numbers, the observations are
290 available of 1 hour. Thus through hourly update along with hourly model advances, the spatially sparse
observations can sufficiently constrain the CO₂ flux, which can be demonstrated by the results. Given
the EnKF algorithm, the posterior uncertainty is proportional to the prior uncertainty but with a smaller
magnitude. Based on hourly update, the posterior uncertainty contains the same flow-dependent
information as the prior uncertainty. For both chemistry assimilation and numerical weather prediction,
295 it is commonly that the dimension of observation is much smaller than the dimension of state vector.
Thus data assimilation helps to use the limited observations to constrain the state vector.

Before being applied in assimilation, the GOSAT retrievals were operated in three steps. First, the Only
data retrievals tagged with “RetrievalResults/outcome_flag =1” were selected, which indicates the
300 retrieval quality. Second, to achieve the most extensive spatial coverage with the assurance of using the
best quality data available, a thinning strategy was used when multiple observations appeared in the same
model grid point at the same hour on each day after interpolation of the model’s horizontal coordinates.
Only retrievals with the minimum value of uncertainty, i.e., “RetrievalResults/xco₂_uncert”, were
selected. Third, OMB quality control method is used to check the background fields to maintain stability
305 in the assimilation. The records with absolute biases (i.e., $|o - b|$) greater than 5 ppm were removed,
which are considered to have a lack of regional representativeness, and was mostly found near the
boundary of the model domain. Moreover, the retrievals for the glint soundings over oceans have
relatively larger uncertainty, and thus many data over oceans were excluded in our inversions in terms of

data screening strategy (Fig. 2).

310

Non-assimilated XCO₂ observations were used for verification purposes after another process of repeated sifting, whose steps were as follows: (1) observations were marked with “outcome_flag = 1”, (2) XCO₂ values with the minimum “xco₂_uncert” in the same model grid point and at the same hour were excluded, which filtered out all of the assimilated XCO₂; (3) outliers were precluded if the $|o - b|$ was larger than
315 5.00 ppm.

2.4 Experimental design and evaluation method

Following previous GOSAT inversion work (Maksyutov et al., 2013; Feng et al., 2017; Wang et al., 2019; Liu et al., 2021; Jiang et al., 2022), in this study, the natural flux (i.e., biosphere–atmosphere exchange and ocean–atmosphere exchange) were optimized, while the fossil-fuel and biomass-burning fluxes were
320 kept unchanged. This design, in which the natural fluxes were a subset of the state variables, further allowed us to focus on investigating the uncertainty of China’s carbon sink, since the uncertainty in prescribed biomass-burning and fossil-fuel emissions are minor compared to that of the biosphere fluxes in the model domain (van der Werf et al., 2017; Zheng et al., 2018; Kurokawa et al., 2020). Fully reconciling the differences between bottom-up and inversion-estimated fossil-fuel emissions is outside
325 the scope of this work and is therefore not discussed any further in this study. Consequently, the selected XCO₂ observations were assimilated hourly to adjust the CO₂ concentrations and fluxes. The assimilation was performed for the period 0000 UTC 25 December 2015 to 2300 UTC 31 December 2016, using the perturbed initial conditions and boundary conditions by adding Gaussian random noise with a standard deviation of 5%. The first 7 days were set as spin-up, which has been testified by Peng et al. (2015) with
330 pseudo-satellite-observation and CMAQ assimilation. Results for the period 1 January to 31 December 2016 are discussed and validated in detail in this paper.

Then, additionally, to assess the quality of the inversion results, two sets of forward simulations were performed throughout the year of 2016. One set of experiments was forced by the optimized *a posteriori*
335 fluxes (denoted as FC), and the other was forced by the prescribed *a priori* fluxes as a control experiment (denoted as CTRL). Both forward runs used the same initial and boundary concentrations from the CT2019B product. Generally, it is hard to validate the optimized flux, because comparison with *in situ*

flux measurements is difficult on account of the discrepancy in scales between fluxes assimilated in the model grid point and eddy-covariance measurements over a very large uniform underlying surface.

340 Therefore, this traditional approach was adopted as a compromise to assess whether the *a posteriori* fluxes would enable improvements in the fit to observed CO₂ concentrations, including non-assimilated GOSAT as well as surface observations from 14 sites.

3 Results

3.1 Performance of observational and analysis increments

345 We begin by analyzing the observational and analysis increment performance of JDAS. According to the statistics listed in Table 1, the total number of assimilated XCO₂ values in 2016 reached 15264 (i.e., 79.22% of the thinned amount), with the monthly ratio of “assimilated-to-thinned” ranging from 74.19% (in August) to 98.91% (in July). The available XCO₂ data amount for JDAS decreases from 1788 in January, to 1870 in February, to 734 in June, and to 728 in July, which represents an approximate 61%
350 reduction in the year-round monthly comparison. Also, it should be noted that the maximum median XCO₂ uncertainty occurred in July (0.99 ppm) and the minimum in December (0.64), indicating a better quality of XCO₂ retrievals in winter and less stable retrievals in summer. As shown in Table 1, both the mean absolute error (MAE) and root-mean-square error (RMSE) exhibit a maximum in July (1.99 ppm and 2.41 ppm, respectively) and a minimum in April and September (MAE: 1.76 and 1.76 ppm; RMSE:
355 2.18 and 2.15 ppm), indicating that the point-by-point uncertainty is larger in summer and lower in spring and autumn, which is consistent with previous model studies (Li et al., 2017). The difference in seasonal performance could be partly due to the uncertainties in the spatial and temporal variations of the biosphere flux estimation and fossil-fuel inventories.

360 Fig. 2 demonstrates the distribution of XCO₂ observation increments and CO₂ flux analysis increments (i.e., the analysis-minus-background $E^a - E^b$) over the model domain, including January (Figs. 2a and b), July (Figs. 2c and d) and the whole year (Figs. 2e and f). In particular, most of the available XCO₂ in July appears in the north and central region of China, but the south and northwest tend to be blank. The XCO₂ innovation range is usually between -3 and 3 ppm in the corresponding model grid point,
365 with a monthly mean value between -0.12 and -0.96 ppm over the model domain. Moreover, the pattern

of CO₂ flux analysis increments (i.e., AN–FC flux) preserve features from innovations and certifies that GOSAT XCO₂ is effectively absorbed in JDAS. GOSAT retrievals were found to display impacts within a certain range near the observation points after entering the assimilation system. The higher variation in monthly flux analysis increments for July than those for January indicates that the uncertainties of forecast flux in summer are larger than those of the variation in winter. Considering the peculiarities of atmospheric CO₂, such as its long atmospheric lifetime, long-range transport, high background concentrations, and strong biosphere–atmosphere exchanges, there are both wide-ranging overall increases (e.g., –0.01 to 0.1 over central China) and decreases (e.g., –0.2 to –0.01 over South China) and small-scale adjustment taking place in 2016 (Fig. 2f).

3.2 Size of the annual carbon sink in China

Before presenting *a posteriori* biosphere fluxes in China from JDAS, Table 2 provides an overview of most of the well-known inversion modeling systems, configurations of inversions, atmospheric transport models, spatiotemporal resolutions, and observations. The inversion systems differ by the transport model, the inversion approach, the choice of observation and prior constraints, enabling us to facilitate the international comparison and mutual recognition. For example, either *in situ* CO₂ or GOSAT XCO₂ constrained flux (i.e., –1.11 and –0.83 PgC yr^{–1}) demonstrates much higher sink estimates from GEOS-Chem-based inversion with a 4° × 5° horizontal resolution. Excluding the outliers, most global inversions report a carbon sink in China of –0.27 to –0.56 PgC yr^{–1} from *in situ* CO₂, and –0.34 to –0.68 PgC yr^{–1} from satellite retrievals. In contrast, our estimates constrained by GOSAT observation (–0.47 PgC yr^{–1}) agree reasonably well with the previous estimates mentioned above.

3.3 Regional characteristics of posterior fluxes

As can be seen in Fig. 3a, the annual horizontal distribution patterns of biosphere flux show significant spatial heterogeneity and fairly large gradients in most areas. Fig. 3b further illustrates annual differences between *a priori* and *a posteriori* fluxes over the model domain. Although China’s total carbon sink of *a posteriori* fluxes (–0.47 PgC yr^{–1}) are approximately equal to the *a priori* fluxes (–0.43 PgC yr^{–1}), the spatial distribution has been modified through assimilation. Compared to the prescribed *a priori* biosphere flux, not only large-scale vegetation adjustments but also small-scale conditions can be detected throughout the year after assimilating atmospheric observations (Fig. 3b). Generally, the *a priori*

395 biosphere fluxes are overestimated ($\sim 0.1\text{--}0.3 \mu\text{mole m}^{-2} \text{s}^{-1}$) in the north (dominated by forest, grassland and cropland) and south (dominated by forest and grassland) of China, while they are underestimated ($\sim 0.1\text{--}0.5 \mu\text{mole m}^{-2} \text{s}^{-1}$) primarily in central China where there is a large area of cropland.

Figs. 3c–f show the seasonal spatial differences before and after assimilation, taking January, April, July and October as representatives of winter, spring, summer and autumn. The monthly averages were
400 calculated from the daily averages based on hourly outputs. The difference between the analysis and prior flux tends to be larger in July, lower in April and October, and lowest in January, which indicates a larger uncertainty in biosphere flux estimates in the growing season. This is consistent with the findings of previous studies (Jiang et al., 2016; Chen et al, 2021; Fu et al., 2022). Moreover, it should be noted that an obvious underestimation of *a priori* flux (approximately $0.1\text{--}0.5 \mu\text{mole m}^{-2} \text{s}^{-1}$) occurs in the northern,
405 central and southern vegetation growth regions. On the other hand, the central part of China, dominated by cropland, shows relatively larger *a posteriori* flux in winter and smaller *a posteriori* flux in summer and autumn, in contrast with the *a priori* flux constrained by the limited background observation sites (Zhang et al., 2014; Jacobson et al., 2020). Additionally, compared with the weekly temporal resolution of global inversion, the hourly observational increments as well as the hourly first-guess fields in this
410 study hold some advantage in evaluating the monthly variations of fluxes. As expected, some distinguishing features are thus demonstrated in the assimilated fluxes, such as the carbon sources in parts of central, eastern and southwest China, which is more consistent with the underlying surface situation. In this way, the JDAS inversion system has the potential to depict the fine-scale characteristics of biosphere flux.

415 Next, we analyze the monthly and annual fluxes in five large regions—west, north, central, south, and mainland China (denoted by the red frame in Fig. 3a)—to analyze the regional inversion in subcontinental-scale flux variation as well as to contrast with the previous inversion analysis (Fig. 4). Given the representative background and observation information, the seasonality patterns were modified
420 by JDAS assimilation, with larger annual sinks relative to the *a priori* ones and a growing season that is shifted earlier in the year over central and south China. As shown in Fig. 4, there is an evident difference in the *a posteriori* annual carbon sink magnitude in these regions, gradually decreasing in the north (e.g., forest, grassland and cropland), south (e.g., forest and grassland), west (e.g., grassland and tundra), and

central region (e.g., cropland) in turn, which is consistent with the primary corresponding ecosystem
425 types, while the *a priori* sink of the west tends to be larger than that of the south. Using the north as a
reference, the annual carbon sink of the *a priori* estimates for the north, south, west and central regions
are 1.00, 0.57, 0.62 and 0.44, respectively, while those of the *a posteriori* estimates are 1.00, 0.62, 0.56
and 0.38. On the other hand, the *a priori* and *a posteriori* amplitudes of the seasonal variation [i.e., the
430 difference between the maximum and minimum monthly estimates, as defined in Scrowell et al. (2016)]
range from 374.33/333.74, 87.01/80.41, 120.33/113.98, 82.34/88.00 to 413.17/389.48 TgC month⁻¹ in
north, south, west, central and mainland China, respectively. Moreover, the drastic fluctuation in the daily
variation of prior fluxes has been modified by observational constraints in JDAS (sub-graph in the left-
hand panel of Fig. 4). Therefore, this implies the potential for regional inversion in interpreting
underlying processes in large regions such as China where the ecosystems and climate are quite varied.

435

Nevertheless, achieving robust and reliable flux signals at smaller regional scales is quite demanding and
rather challenging, because of the limited observations and low accuracy of transport models as well as
the *a priori* information. In this paper, we further try to investigate the condition of the regional biosphere
carbon sink over several of China's key ecological areas (denoted by the blue frame in Fig. 3a)—for
440 example, Daxing'anling (DX), the Loess Plateau (HT), the Qinling Mountains (QL), the rocky desert in
Guangxi (SM), Mount Wuyi (WY), and Xishuangbanna (XS). These regions are characterized by their
unique vegetation and climatic conditions. In particular, the *a priori* and *a posteriori* seasonal amplitudes
amount to 43.64/39.56, 24.03/23.39, 35.73/37.96, 29.36/31.80, 2.70/3.64 and 7.93/7.04 TgC month⁻¹ in
DX, HT, QL, SM, WY and XS, respectively. The DX region is characterized by abundant forest and far
445 more satellite retrievals to constrain fluxes, with annual *a priori* and *a posteriori* carbon sinks of
-25.13/-29.64 TgC yr⁻¹. Compared to *a priori* fluxes, relatively stronger *a posteriori* sinks are also found
in QL (-60.05/-62.53 TgC yr⁻¹), SM (-62.10/-71.27 TgC yr⁻¹), WY (0.36/-2.19 TgC yr⁻¹) and XS
(-10.12/-10.79 TgC yr⁻¹), which is consistent with the improved ecological conditions due to ecological
engineering construction as well as generally favorable climatic conditions. As can be seen in Fig. 5, the
450 XS region is unique and worthy of attention in contrast to the other regions not only because it shows
different seasonality in its release of CO₂ to the atmosphere in summer and removal of CO₂ from the
atmosphere in other seasons, but also because of the large transport model errors that are included in the
model-data mismatch error involved in previous inversion studies (Wang et al., 2020; He et al., 2022;

Schuh et al., 2022; Wang et al., 2022). Thus, the abovementioned spatial variations of *a posteriori* fluxes
455 might unlock some of the potential local signals in areas where regional transport models are more
reliable and observations are plentiful.

3.4 Provincial patterns of optimized fluxes

In this section, we investigate the provincial patterns of biosphere flux (Fig. 6). Based on the gridded *a*
posterior flux dataset, we first assess the annual CO₂ biosphere sink levels in 31 provinces in mainland
460 China (Taiwan, Hong Kong, Macao and Shanghai are not discussed because of the insufficient grid
resolution). At this scale, both the *a priori* and *a posteriori* fluxes indicate the strongest carbon sink
intensity per unit area being in Shaanxi, Guangxi and Guizhou, but the *a priori* fluxes produce an
underestimation in Shanxi and overestimations in Guangxi and Guizhou, respectively. Next, the second
strongest carbon sink intensity is commonly seen in Shaanxi, Sichuan, Chongqing and Hubei, whereas a
465 comparatively low level of carbon sink intensity appears in Xinjiang, Liaoning, Anhui and Yunnan as
well as in Tibet and Fujian. Furthermore, some provinces with neutral (i.e., close to 0), source or sink
statuses are re-evaluated by the GOSAT constrained fluxes (Figs. 6a and b). For instance, the *a posteriori*
flux in Ningxia is $-0.01\text{--}0.01\ \mu\text{mole m}^{-2}\ \text{s}^{-1}$, while the *a priori* flux displays a weak carbon sink of -0.01
to $-0.05\ \mu\text{mole m}^{-2}\ \text{s}^{-1}$, due to the complexity in the estimation related to the grassland and cropland land
470 surfaces in this province. On the contrary, the *a priori* fluxes in Fujian and Jiangsu are close to 0, but we
find a carbon sink ranging from approximately -0.01 to $-0.05\ \mu\text{mole m}^{-2}\ \text{s}^{-1}$ and a carbon source from
 0.05 to $0.1\ \mu\text{mole m}^{-2}\ \text{s}^{-1}$, respectively. For Liaoning, the *a priori* fluxes are characterized by CO₂ sources
($0.01\text{--}0.05\ \mu\text{mole m}^{-2}\ \text{s}^{-1}$), while the assimilated fluxes with satellite measurements are slightly adjusted
to a carbon sink ($-0.05\text{--}0.1\ \mu\text{mole m}^{-2}\ \text{s}^{-1}$).

475

Lastly, the sizes of the provincial biosphere fluxes are summarized and sorted quantitatively in Fig. 7.
The maximum and minimum provincial biosphere flux sizes are in Inner Mongolia (*a posteriori*: -53.65
TgC yr⁻¹; *a priori*: -53.41 TgC yr⁻¹) and Shandong (*a posteriori*: 5.99 TgC yr⁻¹; *a priori*: 3.05 TgC yr⁻¹),
respectively. Moreover, the difference between the *a posteriori* and *a priori* provincial flux ranges from
480 -7.03 TgC yr⁻¹ in Heilongjiang to 2.95 TgC yr⁻¹ in Shandong, with an underestimation greater than 2.00
TgC yr⁻¹ appearing in Shandong (2.95), Jiangsu (2.31) and Hebei (2.25), and an overestimation greater
than 5.00 TgC yr⁻¹ appearing in Heilongjiang (7.03), Liaoning (5.68), Yunnan (5.59) and Guangxi (5.10).

On the other hand, a smaller percentage of modification between the *a posteriori* and *a priori* flux [i.e. $(a\ posteriori - a\ priori) / a\ priori \times 100\%$ in absolute value] arises in Xinjiang (0.28%), Inner Mongolia (0.46%), Tibet (1.10%), Qinghai (2.45%), Gansu (3.21%), Shaanxi (3.50%), Sichuan (4.34%) and Shanxi (4.65%), indicating a lower level of uncertainty in these larger carbon-sink provinces. Nevertheless, an increased percentage of modification in provincial flux appears in Jiangsu (*a posteriori*: 2.29 TgC yr⁻¹; *a priori*: -0.02 TgC yr⁻¹), Liaoning (*a posteriori*: -4.27 TgC yr⁻¹; *a priori*: 1.40 TgC yr⁻¹), Fujian (*a posteriori*: -1.15 TgC yr; *a priori*: 0.29 TgC yr⁻¹), and Shandong (already listed above).

490 3.5 Evaluation against observations

We further assess the performance of the *a posteriori* CO₂ fluxes by comparing the CTRL, FC and AN results in the fit to non-assimilated GOSAT as well as surface observations. The monthly and annual statistics were computed from the hourly outputs from the assimilation, simulation and observations. Table 1 demonstrates (as expected) that the concentration from the analysis fields (AN) performs best when fitted to the non-assimilated XCO₂ observations. It is notable that the column-averaged satellite signals have limited capacity in facilitating the tropospheric variation in CO₂ concentration compared to surface observations. Thus the response to changes in the simulated XCO₂ signal is weak, and improvement is rather moderate. For instance, the annual RMSE, MAE and correlation coefficient for AN are 2.34 ppm, 1.93 ppm and 0.73; for FC, they are 2.63 ppm, 2.02 ppm and 0.66; and for CTRL, they are 2.65 ppm, 2.03 ppm and 0.66, respectively. Additionally, the AN, FC and CTRL biases from non-assimilated XCO₂ observations are further calculated (Table 3), and the outliers in CTRL have been effectively amended. When FC is compared with the CTRL results, the frequency of bias in [-4, 4] increases by 0.25%, in [-3, 3] by 0.36%, in [-2, 2] by 0.32%, and in [-1, 1] by 0.14%. The error standard deviation decreases from 2.63 ppm in CTRL to 2.61 ppm in FC and to 2.27 ppm in AN.

505

Furthermore, surface *in situ* observations from 14 sites are further used as independent observations to evaluate the inversion results. The modeled CO₂ concentrations were extracted from the simulated hourly CO₂ fields according to the locations, elevation, and time of each observation. The averages of observation, CTRL, FC, and AN over these 14 stations are 410.97, 413.01, 412.82, and 412.21 ppm, respectively. The statistics of the analytical field (AN) in Table 4 are better than FC and CTRL, including RMSE and MAE, which gives a direct indication that the assimilation performs well. Taking

510

improvement rate as example, the RMSE improvement rate between the FC and CTRL mostly ranges from -2.13% to 12.34% with an average of 2.48% , and the MAE improvement rate ranges from 0.08% to 9.73% with an average of 2.37% . Although the RMSE and MAE of AN are lower than CTRL and FC, those of FC are higher than CTRL in Lin'an (in Wuhan, Hubei) and Jinsha (in Yangtze River Delta), which are in the vicinity of urban clusters with increased human activity (Liang et al., 2023). Thus, this helps to check that the inversions actually improve the model fits to the observations but also to determine whether some sites are particularly problematic for natural flux inversions. Inversions actually improve the model fits to the surface observations in forest areas (in Northeast, East and Southeast China), cropland areas (in North China), grassland areas (in Mongolia), Ocean (in Korea and Japan) and coastal areas (in Korea).

The annual-averaged horizontal distributions of CO_2 concentration near the surface in 2016 are presented (Fig. 8). Fig. 8a displays the surface CO_2 concentration analysis fields (AN), and the much-refined description in the AN allows for a more detailed characterization of the spatiotemporal distribution of CO_2 concentration and can further facilitate an interpretation of satellite data in a regional context over China. Thus, the AN can be used as a closer representation of the real condition. As shown in Figs. 8b and c, compared to the CTRL fields, the FC fields tend to be considerably closer to the AN fields, suggesting that *a posteriori* fluxes are calibrated acceptably. Furthermore, Fig. 8d shows the year-round statistic of XCO_2 error reduction [defined as $(1 - \delta_{\text{FC}} / \delta_{\text{CTRL}}) \times 100\%$], as well as the amounts of non-assimilated XCO_2 observations, where δ_{FC} represents the FC XCO_2 error standard deviation and δ_{CTRL} the CTRL XCO_2 error standard deviation. The region of $8^\circ\text{--}57^\circ\text{N}$ and $105^\circ\text{--}120^\circ\text{E}$ is used as a reference because there is a relatively larger difference between the *a priori* and *a posteriori* fields, including the concentration as well as flux. In general, the error reduction is primarily found to be positive and ranges from approximately 0.80% to 32.13% with a median of 5.65% and mean of 7.23% . This zonal evaluation further verifies the improvement in the *a posteriori* flux compared to the *a priori* flux.

4 Discussion

4.1 China's carbon sink international comparability among different methods

The total annual carbon sink in previous research along with our study are summarized (Table 2). The

540 aim is mainly to check that different methods—for instance, inventories, ecosystem process models, and atmospheric inversions—actually improve the carbon sink international comparability and mutual recognition. Based on national ecosystem inventory data, China’s terrestrial carbon sink increased from $-0.18 \text{ PgC yr}^{-1}$ in the 1980s to $-0.33 \text{ PgC yr}^{-1}$ in the 2000s owing to forest area expansion and afforestation during recent years (Piao et al, 2009; Jiang et al., 2016; Wang et al., 2022). Meanwhile, the
545 results from several ecosystem process-based models display a carbon sink ranging from -0.13 to $-0.22 \text{ PgC yr}^{-1}$ during 1980–2010, achieved by assessing the effect of changes in climate and CO_2 (Piao et al, 2009; He et al., 2019). In addition, according to the flux gap between top-down and bottom-up estimations mentioned above, a recent estimate of the lateral flux for China is $-0.14 \text{ PgC yr}^{-1}$, which include the carbon exchange between the land and atmosphere in non- CO_2 forms as well as the imported
550 wood and crop products (Wang et al., 2022).

The terrestrial carbon sink in 2016 with lateral fluxes adjustment amounts to approximately $-0.33 \text{ PgC yr}^{-1}$, constrained by the GOSAT XCO_2 in JDAS ($-0.47 \text{ PgC yr}^{-1}$). Correspondingly, we also provide a corrected carbon sink estimate of $-0.54 \text{ PgC yr}^{-1}$ (i.e., $-0.68 + 0.14 = -0.54$) inferred from *in situ* CO_2
555 data provided by JDAS (Peng et al., 2023), which is the optimal mathematical solution under the current sparse observational coverage with daytime photosynthetic uptake, and likely leads to a slight overestimation to some extent. Hence, our estimates (-0.68 and $-0.47 \text{ PgC yr}^{-1}$ from *in situ* CO_2 and GOSAT, respectively) agree reasonably well with the previous estimates mentioned above.

4.2 To what extent the JDAS’s posterior flux is different from prior flux?

560 In general, most research into the inversion of China’s carbon sink has commonly used global transport models. The limited resolution and distribution of observations are deemed to lead to large uncertainties in inversion in small regions, especially at national scales (Scrowell et al., 2019; Monteil et al., 2020; Piao et al., 2022). The resolution-related performance of transport models tends to magnify the uncertainty in China’s carbon sink estimates. For instance, Fu et al. (2022) found that the results of global
565 model (i.e., GEOS-Chem) tended to be generally lower than GOSAT’s XCO_2 in China from the various terrestrial models with a mean bias of about 2 ppm in winter, while Lei et al. (2014) found GEOS-Chem simulations tended to produce higher values than GOSAT (by 5.8 ppm) in China during summer. In contrast, the observational increments of JDAS show an ability to depict the fine-scale features with

strong spatial heterogeneity whilst in general retaining the large-scale spatial patterns, which can be
570 attributed to the CMAQ simulation performance in differentiating the nuances of anthropogenic and
natural conditions. On the other hand, the analysis increments depend not only on the innovations, but
also on how well the Kalman gain matrix computes the contribution weighting factors based on the time-
dependent forecast error covariance. The biosphere flux first-guess fields were derived from the novel
flux forecast model by taking the *a priori* flux, the analysis flux from the previous assimilation cycle,
575 and the forecast concentration (Equation 1), which is a great help in assisting with improving the
background information and initial perturbation for ensemble forecasting.

The good response of the vegetation condition to the *a posteriori* results provides a strong foundation for
a meaningful interpretation of biosphere fluxes. Satellites, with their better spatial coverage, as well as
580 regional transport models, with their improved stability, can help in assessing the real conditions of local
terrestrial ecosystems with complex conditions, such as over central China. The decreased annual sink
and increased seasonal variability in central China deduced by the *a posteriori* flux with satellite may in
fact reflect the atmospheric CO₂ fixed by cropland vegetation, where ~60% of the area is cropland with
relative few *in situ* observations used for constraining the *a priori* flux (Piao et al., 2009, 2022). Actually,
585 downward correction over forest and grassland and upward correction for cropland areas has been
validated against independent data. Inversions actually improve the model fits to the surface observations
in cropland, forest and grassland areas. In general, (1) widespread underestimation of the *a priori* flux
(0.01–0.1 $\mu\text{mole m}^{-2} \text{s}^{-1}$) is found in central China, which is dominated by cropland and where dense
satellite retrievals are accordingly available; (2) overestimates are distributed in the northeast and south
590 of China over a considerable spatial extent; and (3) smaller changes between *a posteriori* and *a priori*
estimates are primarily located in the west of China, which tends to agree with the XCO₂ OMB pattern.
Nevertheless, summer is the season with the largest percentage of satellite data rejection and retrieval
uncertainty, making it a tough test still for inversion systems.

595 At the provincial scale, the provinces in China differ in both the terrestrial vegetation and anthropogenic
activity. As discussed earlier, the difference between *a posteriori* and *a priori* estimates is closely related
to the degree of human activity intervention. Several factors could account for the provincial spatial
distribution constrained from GOSAT; for instance, the increased precipitation along with the strong El

Niño in 2016, the levels of reforestation and afforestation, and the reductions in biofuels in rural areas
600 bringing about a shrubland carbon sink.

4.3 How well can JDAS inversion constrain the carbon sink of China?

Quantitative information on to what extent the posterior fluxes are constrained by observations have been
further checked. The prior information has been embodied in *a priori* flux simulated concentrations, and
observation information has been embodied in the *a posteriori* flux simulation, whose fluxes are
605 constrained by observations. By evaluating the differences between these two sets of simulation results,
the prior information and observation information now have access to be accessed quantitatively. At the
site scale (Table 4), some sites tend to systematically be poorly fitted by the inversions, in particular those
in the vicinity of large urban areas with large anthropogenic emissions, such as Jinsha and Lin'an. Besides
these two sites, the difference between CTRL and FC is affected by the observation information through
610 assimilation ranges from 0.25% to 12.34% (i.e. RMSE decreasing rates), with an average of 2.48%
among all surface observation sites. According to the statistics, the observations have played a positive
role in improving carbon sink over the model domain. The non-assimilated GOSAT XCO₂ has been also
used to assess the difference between prior and posterior flux simulation. The decrease in the misfits is
rather moderate (Table 1).

615

In addition, smaller correlation coefficient improvement in the contrast of CTRL and FC imply that prior
flux patterns play an important role in posterior flux. On the other hand, favorable meteorological
conditions [e.g., precipitation in the growing season being 20% higher than that in 2015 (China Climate
Bulletin 2016)] have also been reported, which further supports the improved ecological quality,
620 indicating JDAS's potential in tracking biosphere CO₂ fluxes from space.

5 Summary and Outlook

Top-down estimations of carbon budgets have been included in the UNFCCC's MVS framework. At
present, most carbon sink inversions in China utilize a global transport model with relatively coarse
resolution. Characterized by large heterogeneity in its biospheric spatiotemporal distribution, the
625 transport model error, as well as the sparseness of *in situ* observations, leads to large uncertainties in the
assimilation of carbon flux in China. In this study, a regional high-resolution inversion model (JDAS)

was used, which has been extended to incorporate GOSAT constraints, along with a joint assimilation of CO₂ flux and concentration at high spatial (64 km) and temporal (1 h) resolution. The annual, monthly and daily variation in biosphere flux was reproduced reasonably well, which was attributable to the novel
630 flux forecast model with diurnal variation, the reliable CMAQ background simulation, carefully chosen XCO₂ retrievals, and the well-designed EnKS assimilation configuration.

The size of the biosphere carbon sink in China amounted to $-0.47 \text{ PgC yr}^{-1}$ with JDAS by GOSAT constraints, which is comparable with previous global estimates (i.e., -0.27 to $-0.56 \text{ PgC yr}^{-1}$ from *in situ* observations and -0.34 to $-0.68 \text{ PgC yr}^{-1}$ from satellite retrievals). Next, the much-refined CMAQ
635 resolution in JDAS inversion was found to allow for a more detailed characterization of the spatiotemporal distribution of CO₂ and to further facilitate an interpretation of carbon flux in a regional context over China. The *a priori* and *a posteriori* seasonal amplitudes ranged from 374.33/333.74, 87.01/80.41, 120.33/113.98, 82.34/88.00 to 413.17/389.48 TgC month⁻¹ in north, south, west, central
640 and mainland China, respectively. Also, the drastic fluctuation in the daily variation of *a priori* fluxes was modified by observational constraints, which appeared more realistic than that of the *a priori* estimates. Moreover, we further investigated the condition of the biosphere carbon sink in several of China's key ecological areas. Using XS as an example, the large transport model errors that were included in the model–data mismatch error involved in previous global inversion studies were effectively reduced
645 by JDAS, and XS was reported to be a relatively stronger sink in contrast to prior estimates ($-10.12/-10.79 \text{ TgC yr}^{-1}$). Furthermore, the provincial patterns of biosphere flux were investigated and re-estimated. As seen from GOSAT, the difference between the *a posteriori* and *a priori* provincial flux ranged from $-7.03 \text{ TgC yr}^{-1}$ in Heilongjiang to 2.95 TgC yr^{-1} in Shandong. Finally, an evaluation against non-assimilated XCO₂ and surface observations demonstrated better performance of the *a posteriori* flux
650 when fitted to the observations, indicating improved results in the regional inversion. Considering our prior estimates from CT2019B, the discrepancy could be because our study (a) relied on a fine-scale regional transport model; (b) was constrained by GOSAT XCO₂ retrievals with better spatial coverage rather than sparse and inhomogeneous *in situ* observations; (c) performed a joint assimilation of CO₂ flux and concentration, which helped reduce the uncertainty in both the initial CO₂ fields and the fluxes; and
655 (d) carried out hourly assimilation based on hourly simulation and observation, which was more realistic.

The regional inversion methodology and results presented here prove the feasibility and superiority of regional CTMs and satellite observations in investigating China's carbon sink. On account of the obvious interannual variation in the biosphere sink, this work also serves as a foundation for future multi-year retrospective analyses of biosphere-atmosphere exchanges under different meteorological conditions. On the one hand, although the ACOS retrieval technology has been substantially improved and provides unprecedented spatial coverage, more XCO₂ retrievals with better quality and lower retrieval uncertainty are still needed, especially during summertime as well as over ocean and west China. On the other hand, a knowledge gap also exists in inversion-based estimates, in which fossil-fuel emissions are generally assumed to be accurate. Besides uncertainties in natural flux, our current knowledge of urban emissions is far from adequate. Around 70% of fossil-fuel emissions are derived from cities in combination with considerable uncertainties. Within the framework of the Paris Agreement, inversions at higher spatial resolution are an increasing demand, making it crucial to develop the capacity for inversions to quantify urban emissions and assess the effectiveness of emission mitigation strategies, alongside calls for improvements in observations, *a priori* information, anthropogenic emission inventories, transport models, and inversion technology.

Acknowledgements

The authors are grateful to the two anonymous reviewers for their precious suggestions. This work was supported by the National Key Scientific and Technological Infrastructure project "Earth System Science Numerical Simulator Facility" (EarthLab). This work was also sponsored by the National Natural Science Foundation of China through Grants 41875014 and 42275153. In addition, this work was supported by State Key Laboratory of Atmospheric Boundary Layer Physics and Atmospheric Chemistry (LAPC-KF-2022-01) and Key Laboratory of South China Sea Meteorological Disaster Prevention and Mitigation of Hainan Province (SCSF202208)

Data Availability

The GOSAT retrievals were produced by the ACOS/OCO-2 project at the Jet Propulsion Laboratory, California Institute of Technology, and obtained from the JPL website, co2.jpl.nasa.gov. The CarbonTracker CT2019B provided by NOAA ESRL, Boulder, Colorado, USA is available from

685 <http://carbontracker.noaa.gov>. Data analysis is done with the Matlab version 2019b (MATLAB and Statistics Toolbox Release, 2019b, mathworks.com) and the Gridded Analysis and Display System (GrADS; <http://cola.gmu.edu/grads/>) [Software].

Competing interests

The contact author has declared that neither they nor their co-authors have any competing interests.

690 References

Brioude, J., Angevine, W. M., Ahmadov, R., Kim, S. W., Evan, S., McKeen, S. A., Hsie, E. Y., Frost, G. J., Neuman, J. A., Pollack, I. B., Peischl, J., Ryerson, T. B., Holloway, J., Brown, S. S., Nowak, J. B., Roberts, J. M., Wofsy, S. C., Santoni, G. W., Oda, T., and Trainer, M.: Top-down estimate of surface flux in the Los Angeles Basin using a mesoscale inverse modeling technique: assessing anthropogenic emissions of CO, NO_x and CO₂ and their impacts, *Atmos. Chem. Phys.*, 13, 3661–
695 3677, <https://doi.org/10.5194/acp-13-3661-2013>, 2013.

Broquet, G., Chevallier, F., Rayner, P., Aulagnier, C., Pison, I., Ramonet, M., Martina, S., Vermeulen, A. T., and Ciais, P. A.: European summertime CO₂ biogenic flux inversion at mesoscale from continuous in situ mixing ratio measurements, *J. Geophys. Res.-Atmos.*, 116, D23303,
700 <https://doi.org/10.1029/2011JD016202>, 2011.

Buchwitz, M., Reuter, M., Bovensmann, H., Pillai, D., Heymann, J., Schneising, O., Rozanov, V., Krings, T., Burrows, J. P., and Boesch, H.: Carbon Monitoring Satellite (CarbonSat): assessment of atmospheric CO₂ and CH₄ retrieval errors by error parameterization, *Atmos. Meas. Tech.*, 3477–
3500, <https://doi:10.5194/amt-6-3477-2013>, 2013.

705 Byrne, B., Jones, D. B. A., Strong, K., Zeng, Z. C., Deng, F., and Liu, J.: Sensitivity of CO₂ surface flux constraints to observational coverage, *J. Geophys. Res.-Atmos.*, 122, 6672–6694, <https://doi.org/10.1002/2016JD026164>, 2017

Byrne, B., Jones, D. B. A., Strong, K., Polavarapu, S. M., Harper, A. B., Baker, D. F., and Maksyutov, S.: On what scales can GOSAT flux inversions constrain anomalies in terrestrial ecosystems? *Atmos. Chem. Phys.*, 19, 13017–13035, <https://doi.org/10.5194/acp-19-13017-2019>, 2019.
710

Chen, Z. C., Huntzinger, D. N., Liu, J. J., Piao, S. L., Wang, X. H., and Sitch, S.: Five years of variability

in the global carbon cycle: comparing an estimate from the Orbiting Carbon Observatory-2 and process-based models, *Environ. Res. Lett.*, 16, 054041, <https://doi.org/10.1088/1748-9326/abfac1>, 2021.

715 Chevallier, F.: On the statistical optimality of CO₂ atmospheric inversions assimilating CO₂ column retrievals, *Atmos. Chem. Phys.*, 15, 11133–11145, <https://doi.org/10.5194/acp-15-11133-2015>, 2015.

Chevallier, F., Remaud, M., O’Dell, C. W., Baker, D., Peylin, P., and Cozic, A.: Objective evaluation of surface- and satellite driven CO₂ atmospheric inversions, *Atmos. Chem. Phys.*, 19, 14233–14251, <https://doi.org/10.5194/acp-19-14233-2019>, 2019, 720

China Climate Bulletin 2016. by National Climate Center, China Meteorological Administration.

Ciais, P., Crisp, D., Denier van der Gon, H., Engelen, R., JanssensMaenhout, G., Heimann, M., Rayner, P., and Scholze, M.: Towards a European operational observing system to monitor fossil CO₂ emissions – final report from the expert group, vol. 19, European Commission, Copernicus Climate Change Service, – ISBN 978-92-79-53482-9, doi 10.2788/350433, 2015. Available at: https://www.copernicus.eu/sites/default/files/2018-10/CO2_Report_22Oct2015.pdf. Last access: 1 November 2022. 725

Deng, F., Jones, D. B. A., O’Dell, C. W., Nassar, R., and Parazoo, N. C.: Combining GOSAT XCO₂ observations over land and ocean to improve regional CO₂ flux estimates, *J. Geophys. Res.-Atmos.*, 121, 1896–1913, <https://doi.org/10.1002/2015JD024157>, 2016. 730

Deng, Z., Ciais, P., Tzompa-Sosa, Z. A., Saunio, M., Qiu, C., Tan, C., Sun, T. C., Ke, P. Y., Cui, Y. N., and Tanaka, K.: Comparing national greenhouse gas budgets reported in UNFCCC inventories against atmospheric inversions, *Earth Syst. Sci. Data*, 14, 1639–1675, <https://doi.org/10.5194/essd-14-1639-2022>, 2022.

735 Eldering, A., O’Dell, C.W., Wennberg, P. O., Crisp, D., Gunson, M. R., Viatte, C., Avis, C., Braverman, A., Castano, R., and Chang, A.: The Orbiting Carbon Observatory-2: first 18 months of science data products, *Atmos. Meas. Tech.*, 10, 549–563, <https://doi.org/10.5194/amt-10-549-2017>, 2017a.

Eldering, A., Wennberg, P. O., Crisp, D., Schimel, D. S., Gunson, M. R., Chatterjee, A., Liu, J., Schwandner, F. M., Sun, Y., O’Dell, C. W.: The Orbiting Carbon Observatory-2 early science investigations of regional carbon dioxide fluxes, *Science*, 358, <https://doi.org/10.1126/science.aam5745>, 2017b. 740

- Eldering, A., Taylor, T. E., O'Dell, C. W., and Pavlick, R.: The OCO-3 mission: measurement objectives and expected performance based on 1 year of simulated data, *Atmos. Meas. Tech.*, 12, 2341–2370, <https://doi.org/10.5194/amt-2018-357>, 2019.
- 745 Enting, I. G., Trudinger, C. M., and Francey, R. J.: A synthesis inversion of the concentration and $\delta^{13}\text{C}$ of atmospheric CO_2 , *Tellus B*, 47, 35–52, <https://doi.org/10.3402/tellusb.v47i1-2.15998>, 1995.
- Feng, L., Palmer, P. I., Bösch, H., and Dance, S.: Estimating surface CO_2 fluxes from space-borne CO_2 dry air mole fraction observations using an ensemble Kalman filter, *Atmos. Chem. Phys.*, 9, 2619–2633, <https://doi.org/10.5194/acp-9-2619-2009>, 2009.
- 750 Feng, L., Palmer, P. I., Bösch, H., Parker, R. J., Webb, A. J., Correia, C. S. C., Deutscher, N. M., Domingues, L. G., Feist, D. G., Gatti, L. V., Gloor, E., Hase, F., Kivi, R., Liu, Y., Miller, J. B., Morino, I., Sussmann, R., Strong, K., Uchino, O., Wang, J., and Zahn, A.: Consistent regional fluxes of CH_4 and CO_2 inferred from GOSAT proxy $\text{XCH}_4:\text{XCO}_2$ retrievals, 2010–2014, *Atmos. Chem. Phys.*, 17, 4781–4797, <https://doi.org/10.5194/acp-17-4781-2017>, 2017.
- 755 Friedlingstein, P., O'Sullivan, M., Jones, M. W., Andrew, R. M., Hauck, J., Olsen, A., Peters, G. P., Peters, W., Pongratz, J., Sitch, S., Le Quéré C., Canadell, J. G., Ciais, P., Jackson, R. B., Alin, S., Aragão, L. E. O. C., Arneeth, A., Arora, V., Bates, N. R., Becker, M., Benoit-Cattin, A., Bittig, H. C., Bopp, L., Bultan, S., Chandra, N., Chevallier, F., Chini, L. P., Evans, W., Florentie, L., Forster, P. M., Gasser, T., Gehlen, M., Gilfillan, D., Gkritzalis, T., Gregor, L., Gruber, N., Harris, I., Hartung,
- 760 K., Haverd, V., Houghton, R. A., Ilyina, T., Jain, A. K., Joetzjer, E., Kadono, K., Kato, E., Kitidis, V., Korsbakken, J. I., Landschützer, P., Lefèvre, N., Lenton, A., Lienert, S., Liu, Z., Lombardozi, D., Marland, G., Metzl, N., Munro, D. R., Nabel, J. E. M. S., Nakaoka, S.-I., Niwa, Y., O'Brien, K., Ono, T., Palmer, P. I., Pierrot, D., Poulter, B., Resplandy, L., Robertson, E., Rödenbeck, C., Schwinger, J., Šefrián, R., Skjelvan, I., Smith, A. J. P., Sutton, A. J., Tanhua, T., Tans, P. P., Tian,
- 765 H., Tilbrook, B., van der Werf, G., Vuichard, N., Walker, A. P., Wanninkhof, R., Watson, A. J., Willis, D., Wiltshire, A. J., Yuan, W., Yue, X., and Zaehle, S.: Global carbon budget 2020, *Earth Syst. Sci. Data*, 12, 3269–3340, <https://doi.org/10.5194/essd-12-3269-2020>, 2020
- Fu, Y., Liao, H., Tian, X. J., Gao, H., Jia, B. H., and Han, R.: Impact of prior terrestrial carbon fluxes on simulations of atmospheric CO_2 concentrations, *J. Geophys. Res.-Atmos.*, 126, e2021JD034794, <https://doi.org/10.1029/2021JD034794>, 2021.
- 770 Gaspari, G., & Cohn S. E. Construction of correlation functions in two and three dimensions. *Quarterly*

Journal of the Royal Meteorological Society, 125, 723–757.
<https://doi.org/10.1002/qj.49712555417>, 1999.

775 Glumb, R., Davis, G., and Lietzke, C.: The tanso-fts-2 instrument for the gosat-2 greenhouse gas monitoring mission, 2014 IEEE Geoscience and Remote Sensing Symposium, 1238–1240, <https://doi.org/10.1109/IGARSS.2014.6946656>, 2014.

He, H. L., Wang, S. Q., Zhang, L., Wang, J. B., Ren, X. L., Zhou, L., Piao, S. L., Yan, H., Ju, W. M., Gu, F. X., Yu, S. Y., Yang, Y. H., Wang, M. M., Niu, Z. G., Ge, R., Yan, H. M., Huang, M., Zhou, G. Y., Bai, Y. F., Xie, Z. Q., Tang, Z. Y., Wu, B. F., Zhang, L. M., He, N. P., Wang, Q. F., and Yu, G. R.:
780 Altered trends in carbon uptake in China's terrestrial ecosystems under the enhanced summer monsoon and warming hiatus, *Natl. Sci. Rev.*, 6, 505–514, <https://doi.org/10.1093/nsr/nwz021>, 2019.

He, W., Jiang, F., Wu, M., Ju, W., Scholze, M., Chen, J. M., Byrne, B., Liu, J. J., Wang, H. M., Wang, J., Wang, S. H., Zhou, Y. L., Zhang, C. H., Nguyen, N. T., Shen, Y., and Chen, Z.: China's terrestrial
785 carbon sink over 2010–2015 constrained by satellite observations of atmospheric CO₂ and land surface variables, *J. Geophys. Res. Biogeosci.*, 127, e2021JG006644, <https://doi.org/10.1029/2021JG006644>, 2022.

Houtekamer, P. L., & Mitchell, H. L.: A sequential ensemble Kalman filter for atmospheric data assimilation. *Monthly Weather Review*, 129, 123–137. [https://doi.org/10.1175/1520-0493\(2001\)129<0123:ASEKFF>2.0.CO;2](https://doi.org/10.1175/1520-0493(2001)129<0123:ASEKFF>2.0.CO;2), 2001.
790

Huang, Z. K., Peng, Z., Liu, H. N., Zhang, M. G., Ma, X. G., Yang, S. C., Lee, S. D., Kim, S. Y.: Development of CMAQ for East Asia CO₂ data assimilation under an EnKF framework: a first result, *Chin. Sci. Bull.*, 59, 3200–3208, <https://doi.org/10.1007/s11434-014-0348-9>, 2014.

Houweling, S., Baker, D., Basu, S., Boesch, H., Butz, A., Chevallier, F., Deng, F., Dlugokencky, E. J.,
795 Feng, L., Ganshin, A., Hasekamp, O., Jones, D., Maksyutov, S., Marshall, J., Oda, T., O'Dell, C. W., Oshchepkov, S., Palmer, P. I., Peylin, P., Poussi, Z., Reum, F., Takagi, H., Yoshida, Y., Zhuravlev, R.: An intercomparison of inverse models for estimating sources and sinks of CO₂ using GOSAT measurements, *J. Geophys. Res.-Atmos.*, 120, 5253–5266, <https://doi.org/10.1002/2014JD022962>, 2015.

800 IPCC 2019, 2019 Refinement to the 2006 IPCC Guidelines for National Greenhouse Gas Inventory, Buendia, C. E., Guendehou, S., Limmeechokchai, B., Pipatti, R., Rojas, Y., and Sturgiss, R. (eds).

- Jacobson, A. R., Schuldt, K. N., Miller, J. B., Oda, T., Tans, P., Andrews, A., Mund, J., Ott, L., Collatz, G. J., Aalto, T., et al., 2020. CarbonTracker CT2019B, model published by NOAA Global Monitoring Laboratory, <http://dx.doi.org/10.25925/20201008>. Available at
805 <https://gml.noaa.gov/ccgg/carbontracker/CT2019B/>. Last access: 1 November 2022.
- Jiang, F., Wang, H. M., Chen, J. M., Ju, W. M., Tian, X. J., Feng, S. Z., Li, G. C., Chen, Z. Q., Zhang, S. P., Lu, X. H., Liu, J., Wang, H. K., Wang, J., He, W., and Wu, M. S.: Regional CO₂ fluxes from 2010 to 2015 inferred from GOSAT XCO₂ retrievals using a new version of the Global Carbon Assimilation System, *Atmos. Chem. Phys.*, 21, 1963–1985, [https://doi.org/10.5194/acp-21-1963-](https://doi.org/10.5194/acp-21-1963-2021)
810 2021, 2021.
- Jiang, F., Chen, J. M., Zhou, L. X., Ju, W. M., Zhang, H. F., Machida, T., Ciais, P., Peters, W., Wang, H. M., Chen, B. Z., Liu, L. X., Zhang, C. H., Matsueda, H., and Sawa, Y.: A comprehensive estimate of recent carbon sinks in China using both top-down and bottom-up approaches, *Sci. Rep.*, 6, 22130, <https://doi.org/10.1038/srep22130>, 2016.
- 815 Jiang, F., Ju, W. M., He, W., Wu, M. S., Wang, H. M., Wang, J., Jia, M. W., Feng, S. Z., Zhang, L., Y., and Chen, J. M.: A 10-year global monthly averaged terrestrial net ecosystem exchange dataset inferred from the ACOS GOSAT v9 XCO₂ retrievals (GCAS2021), *Earth Syst. Sci. Data*, 3013–3037, <https://doi.org/10.5194/essd-14-3013-2022>, 2022.
- Kiel, M., Eldering, A., Roten, D. D., Lin, J. C., Feng, S., Lei, R. X., Lauvaux, T., Oda, T., Roehl, C. M.,
820 Blavier, J. F., and Iraci, L. T.: Urban-focused satellite CO₂ observations from the Orbiting Carbon Observatory-3: A first look at the Los Angeles megacity, *Remote Sens. Environ.*, 258, 112314, <https://doi.org/10.1016/j.rse.2021.112314>, 2021
- Kou, X. X., Zhang, M. G., and Peng, Z.: Numerical simulation of CO₂ concentrations in East Asia with RAMS-CMAQ, *Atmos. Oceanic Sci. Lett.*, 6(4), 179–184, [https://doi.org/10.3878/j.issn.1674-](https://doi.org/10.3878/j.issn.1674-2834.13.0022)
825 2834.13.0022, 2013.
- Kou, X. X., Zhang, M. G., Peng, Z., and Wang, Y. H.: Assessment of the biospheric contribution to surface atmospheric CO₂ concentrations over East Asia with a regional chemical transport model, *Adv. Atmos. Sci.*, 32(3), 287–300, <https://doi.org/10.1007/s00376-014-4059-6>, 2015.
- Kou, X. X., Tian, X. J., Zhang, M. G., Peng, Z., and Zhang, X. L.: Accounting for CO₂ variability over
830 East Asia with a regional joint inversion system and its preliminary evaluation, *J. Meteor. Res.*, 31(5), 834–851, <https://doi.org/10.1007/s13351-017-6149-8>, 2017.

- Kou, X. X., Peng, Z., Zhang, M. G., Zhang, N., Lei, L., Zhao, X., Miao, S. G., Li, Z. M., and Ding, Q. J.: Assessment of the meteorological impact on improved PM_{2.5} air quality over North China during 2016–2019 based on a regional joint atmospheric composition reanalysis data-set, *J. Geophys. Res.-Atmos.*, 126, e2020JD034382, <https://doi.org/10.1029/2020JD034382>, 2021.
- 835
- Kountouris, P., Gerbig, C., Rördenbeck, C., Karstens, U., Koch, T. F., and Heimann, M.: Atmospheric CO₂ inversions on the mesoscale using data-driven prior uncertainties: quantification of the European terrestrial CO₂ fluxes, *Atmos. Chem. Phys.*, 18, 3047–3064, <https://doi.org/10.5194/acp-18-3047-2018>, 2018.
- 840
- Kurokawa, J. and Ohara, T.: Long-term historical trends in air pollutant emissions in Asia: Regional Emission inventory in ASia (REAS) version 3, *Atmos. Chem. Phys.*, 20, 12761–12793, <https://doi.org/10.5194/acp-20-12761-2020>, 2020.
- Kuze, A., Suto, H., Nakajima, M., and Hamazaki, T.: Thermal and near infrared sensor for carbon observation Fourier-transform spectrometer on the Greenhouse Gases Observing Satellite for greenhouse gases monitoring, *Appl. Opt.*, 48, 6716–6733, <https://doi.org/10.1364/AO.48.006716>, 2009.
- 845
- Lauvaux, T., Miles, N. L., Deng, A., Richardson, S. J., Cambaliza, M. O., Davis, K. J., Gaudet, B., Gurney, K. R., Huang, J. H., O’keefe, D., Song, Y., Karion, A., Oda, T., Patarasuk, R., Razlivanov, I., Sarmiento, D., Shepson, P., Sweeney, C., Turnbull, J., Wu, K.: High-resolution atmospheric inversion of urban CO₂ emissions during the dormant season of the Indianapolis Flux Experiment (INFLUX), *J. Geophys. Res.-Atmos.*, 121, 5213–5236, <https://doi.org/10.1002/2015JD024473>, 2016.
- 850
- Lei, L., Guan, X., Zeng, Z., Zhang, B., Ru, F., and Bu, R.: A comparison of atmospheric CO₂ concentration GOSAT-based observations and model simulations, *Sci. China Earth Sci.*, 57(6), 1393–1402, <https://doi.org/10.1007/s11430-013-4807-y>, 2014.
- 855
- Lei, R. X., Feng, S., Danjou, A., Grouet, G., Wu, Dien, Lin, J. C., O’Dell, C. W., and Lauvaux, T.: Fossil fuel CO₂ emissions over metropolitan areas from space: A multi-model analysis of OCO-2 data over Lahore, Pakistan, *Remote Sens. Environ.*, 264, 112625, <https://doi.org/10.1016/j.rse.2021.112625>, 2021.
- 860
- Lei, R. X., Feng, S., Xu, Y., Tran, S., Ramonet, M., Grutter, M., Garcia, A., Campos-Pineda, M., and Lauvaux, T.: Reconciliation of asynchronous satellite-based NO₂ and XCO₂ enhancements with

- mesoscale modeling over two urban landscapes, *Remote Sens. Environ.*, 281, 113241, <https://doi.org/10.1016/j.rse.2022.113241>, 2022.
- 865 Li, R., Zhang, M. G., Chen, L. F., Kou, X. X., and Skorokhod, A.: CMAQ simulation of atmospheric CO₂ concentration in East Asia: comparison with GOSAT observations and ground measurements, *Atmos. Environ.*, 160, 176–185, <http://dx.doi.org/10.1016/j.atmosenv.2017.03.056>, 2017.
- Liang, M., Zhang, Y., Ma, Q., L., Yu, D. J., Chen, X. J., Cohen, J. B.: Dramatic decline of observed atmospheric CO₂ and CH₄ during the COVID-19 lockdown over the Yangtze River Delta of China. *J. Environ. Sci.*, 124, 712–722, <https://doi.org/10.1016/j.jes.2021.09.034>, 2023.
- 870 Lindqvist, H., O’Dell, C. W., Basu, S., Boesch, H., Chevallier, F., Deutscher, N., Feng, L., Fisher, B., Hase, F., Inoue, M., Kivi, R., Morino, I., Palmer, P. I., Parker, R., Schneider, M., Sussmann, R., and Yoshida, Y.: Does GOSAT capture the true seasonal cycle of carbon dioxide?, *Atmos. Chem. Phys.*, 15, 13023–13040, <https://doi.org/10.5194/acp-15-13023-2015>, 2015.
- Liu, J. J., Baskaran, L., Bowman, K., Schime, D., Bloom, A. A., Parazoo, N. C., Oda, T., Carroll, D., 875 Menemenlis, D., Joiner, J., Commane, R., Daube, B., Gatti, L. V., McKain, K., Miller, J., Stephens, B. B., Sweeney, C., and Wofsy, S.: Carbon Monitoring System Flux Net Biosphere Exchange 2020 (CMS-Flux NBE 2020), *Earth Syst. Sci. Data*, 13, 299–330, <https://doi.org/10.5194/essd-13-299-2021>, 2021.
- Liu, Y., Wang, J., Yao, L., Chen, X., Cai, Z. N., Yang, D. X., Yin, Z. S., Gu, S. Y., Tian, L. F., Lu, N. 880 M., and Lyu, D. R.: The TanSat mission: Preliminary global observations, *Sci. Bull.*, 63(18), 1200–1207, <https://doi.org/10.1016/j.scib.2018.08.004>, 2018.
- Liu, Z., Bambha, R. P., Pinto, J. P., Zeng, T., Boylan, J., Huang, M. Y., Lei, H. M., Zhao, C., Liu, S. S., Mao, J. F., Schwalm, C. R., Shi, X. Y., Wei, Y. X., Michelsen, H. A.: Toward verifying fossil fuel CO₂ emissions with the Community Multi-scale Air Quality (CMAQ) model: motivation, model 885 description and initial simulation, *J. Air Waste Manage. Assoc.*, 64, 419–435, <https://doi.org/10.1080/10962247.2013.816642>, 2013.
- Maksyutov, S., Takagi, H., Valsala, V. K., Saito, M., Oda, T., Saeki, T., Belikov, D. A., Saito, R., Ito, A., Yoshida, Y., Morino, I., Uchino, O., Andres, R. J., and Yokota, T.: Regional CO₂ flux estimates for 2009–2010 based on GOSAT and ground-based CO₂ observations, *Atmos. Chem. Phys.*, 13, 9351– 890 9373, <https://doi.org/10.5194/acp-13-9351-2013>, 2013.
- Monteil, G., Broquet, G., Scholze, M., Lang, M., Karstens, U., Gerbig, C., Koch, F.-T., Smith, N. E.,

- Thompson, R. L., Lujikx, I. T., White, E., Meesters, A., Ciais, P., Ganesan, A. L., Manning, A.,
Mischurow, M., Peters, W., Peylin, P., Tarniewicz, J., Rigby, M., Rödenbeck, C., Vermeulen, A., and
Walton, E. M.: The regional European atmospheric transport inversion comparison, EUROCOM:
895 first results on European-wide terrestrial carbon fluxes for the period 2006–2015, *Atmos. Chem.
Phys.*, 20, 12063–12091, <https://doi.org/10.5194/acp-20-12063-2020>, 2020.
- Monteil, G., and Scholze, M.: Regional CO₂ inversions with LUMIA, the Lund University Modular
Inversion Algorithm, v1.0, *Geosci. Model Dev.*, 14, 3383–3406, <https://doi.org/10.5194/gmd-14-3383-2021>, 2021.
- 900 Peng, Z., Zhang, M. G., Kou, X. X., Tian, X. J., and Ma, X. G.: A regional carbon flux data assimilation
system and its preliminary evaluation in East Asia, *Atmos. Chem. Phys.*, 15, 1087–1104,
<https://doi.org/10.5194/acp-15-1087-2015>, 2015.
- Peng, Z., Liu, Z., Chen, D., and Ban, J.: Improving PM_{2.5} forecast over China by the joint adjustment of
initial conditions and source emissions with an ensemble Kalman filter, *Atmos. Chem. Phys.*, 17,
905 4837–4855, <https://doi.org/10.5194/acp-17-4837-2017>, 2017.
- Peng, Z., Lei, L., Liu, Z., Sun, J., Ding, A., Ban, J., Chen, D., Kou, X. X., and Chu, K. K.: The impact of
multi-species surface chemical observation assimilation on air quality forecasts in China, *Atmos.
Chem. Phys.*, 18, 17387–17404, <https://doi.org/10.5194/acp-18-17387-2018>, 2018.
- Peng, Z., Lei, L. L., Liu, Z., Liu, H. N., Chu, K. K., and Kou, X. X.: Impact of assimilating meteorological
910 observations on source emissions estimate and chemical simulations, *Geophys. Res. Lett.*, 47,
e2020GL089030, <https://doi.org/10.1029/2020GL089030>, 2020.
- Peng, Z., Kou, X. X., Zhang, M. G., Lei, L. L., Miao, S. G., Wang, H. M., Jiang, F., Han, X., and Fang,
S. X. CO₂ flux inversion with a regional joint data assimilation system based on CMAQ, EnKS, and
surface observations. *J. Geophys. Res.-Atmos.*, 128, e2022JD037154. [https://doi.
915 org/10.1029/2022JD037154](https://doi.org/10.1029/2022JD037154), 2023
- Peters, W., Jacobson, A. R., Sweeney, C., Andrews, A. E., Conway, T. J., Masarie, K., Miller, J. B.,
Bruhwiler, L. M. P., Petron, G., Hirsch, A., Worthy, D. E. J., van der Werf, G. R., Randerson, J. T.,
Wennberg, P. O., Krol, M. C., Tans, P. P.: An atmospheric perspective on North American carbon
dioxide exchange: CarbonTracker, *P. Natl. Acad. Sci. USA*, 104, 18925–18930, [https://doi.org/
920 10.1073/pnas.0708986104](https://doi.org/10.1073/pnas.0708986104), 2007.
- Piao, S. L., Fang, J. Y., Ciais, P., Peylin, P., Huang, Y., Sitch, S. and Wang, T.: The carbon balance of

terrestrial ecosystems in China, *Nature*, 458, 23, 1009–1013, <https://doi.org/10.1038/nature07944>, 2009.

925 Piao, S., He, Y., Wang, X., and Chen F. Estimation of China's terrestrial ecosystem carbon sink: methods, progress and prospects, *Sci. China Earth Sci.*, 65(4): 641–651, <https://doi.org/10.1007/s11430-021-9892-6>, 2022.

Pillai, D., Buchwitz, M., Gerbig, C., Koch, T., Reuter, M., Bovensmann, H., Marshall, J., and Burrows, J. P.: Tracking city CO₂ emissions from space using a high-resolution inverse modelling approach: a case study for Berlin, Germany, *Atmos. Chem. Phys.*, 16, 9591–9610, [https://doi.org/10.5194/acp-](https://doi.org/10.5194/acp-16-9591-2016) 930 16-9591-2016, 2016.

Pinty B., Janssens-Maenhout, G., Dowell, M., Zunker, H., Brunhes, T., Ciais, P., Holmlund, G. Janssens-Maenhout, Y. Meijer, P. and Palmer, M. S.: An Operational Anthropogenic CO₂ Emissions Monitoring & Verification Support capacity - Baseline Requirements, Model Components and Functional Architecture, doi:10.2760/39384, 2017. European Commission Joint Research Centre, 935 EUR 28736 EN

Rödenbeck, C., Zaehle, S., Keeling, R., and Heimann, M.: How does the terrestrial carbon exchange respond to inter-annual climatic variations? A quantification based on atmospheric CO₂ data, *Biogeosci.*, 15(8), 2481–2498, <https://doi.org/10.5194/bg-15-2481-2018>, 2018.

Reuter, M., Buchwitz, M., Hilker, M., Heymann, J., Bovensmann, H., Burrow, J. P., Houweling, S., Liu, 940 Y. Y., Nassar, M. R., Chevallier, F., Ciais, P., Marshall, J., and Reichstein, M.: How much CO₂ is taken up by the European terrestrial biosphere?, *B. Am. Meteorol. Soc.*, 665–671, <https://doi.org/10.1175/BAMS-D-15-00310.1>, 2017.

Schuh, A. E., Byrne, B., Jacobson, A. R., Crowell, S. M. R., Deng, F., Baker, D. F., Johnson, M. S., Philip, S., and Weir, B.: On the role of atmospheric model transport uncertainty in estimating the 945 Chinese land carbon sink, *Nature*, 603, E13–E16, <https://doi.org/10.1038/s41586-021-04258-9>, 2022, arising from Wang et al. *Nature* <https://doi.org/10.1038/s41586-020-2849-9> (2020)

Staufer, J., Broquet, G., Brón, F. M., Puygrenier, V., Chevallier, F., Xueref-Rény, I., Dieudonné E., Schmidt, M. L. M., Ramonet, M., Perrussel, O., Lac, C., Wu, L., and Ciais, P. The first 1-year-long estimate of the Paris region fossil fuel CO₂ emissions based on atmospheric inversion, *Atmos. Chem. Phys.*, 16, 14703–14726, <https://doi.org/10.5194/acp-16-14703-2016>, 2016: 950

Takagi, H., Houweling, S., Andres, R. J., Belikov, D., Bril, A., Boesch, H., Butz, A., Guerlet, S.,

- Hasekamp, O., Maksyutov, S., Morino, I., Oda, T., O'Dell, C., Oshchepkov, S., Parker, R., Saito, M., Uchino, O., Yokota, T., Yoshida, Y., Valsala, V.: Influence of differences in current GOSAT XCO₂ retrievals on surface flux estimation, *Geophys. Res. Lett.*, 41, 2598–2605, 955 <https://doi.org/10.1002/2013GL059174>, 2014.
- Thompson, R. L., and Stohl, A.: FLEXINVERT: an atmospheric Bayesian inversion framework for determining surface fluxes of trace species using an optimized grid, *Geosci. Model Dev.*, 7, 2223–2242, <https://doi.org/10.5194/gmd-7-2223-2014>, 2014.
- Thompson, R. L., Patra, P. K., Chevallier, F., Maksyutov, S., Law, R. M., Ziehn, T., van der Laan-Luijkx, 960 I. T., Peters, W., Ganshin, A., Zhuravlev, R., Maki, T., Nakamura, T., Shirai, T., Ishizawa, M., Saeki, T., Machida, T., Poulter, B., Canadell, J. G. and Ciais, P.: Top-down assessment of the Asian carbon budget since the mid 1990s, *Nat. Commun.*, 7, 10724, <https://doi.org/10.1038/ncomms10724>, 2016.
- Tian, H., Xu, X., Lu, C., Liu, M., Ren, W., Chen, G., Melillo, J., and Liu, J. Net exchanges of CO₂, CH₄, and N₂O between China's terrestrial ecosystems and the atmosphere and their contributions to 965 global climate warming, *J. Geophys. Res.-Atmos.*, 116, G02011, <https://doi.org/10.1029/2010JG001393>, 2011.
- Tian, X., Xie, Z., Liu, Y., Cai, Z., Fu, Y., Zhang, H., and Feng, L.: A joint data assimilation system (Tan-Tracker) to simultaneously estimate surface CO₂ fluxes and 3-D atmospheric CO₂ concentrations from observations, *Atmos. Chem. Phys.*, 14, 13281–13293, [https://doi.org/doi:10.5194/acp-14-](https://doi.org/doi:10.5194/acp-14-13281-2014) 970 13281-2014, 2014.
- UNFCCC 2015. The Paris Agreement on Climate Change, available at <https://www.nrdc.org/sites/default/files/paris-climate-agreement-IB.pdf>. Last access: 1 November 2022
- van der Laan-Luijkx, I. T., van der Velde, I. R., van der Veen, E., Tsuruta, A., Stanislawski, K., 975 Babenhauserheide, A., Zhang, H. F., Liu, Y., He, W., Chen, H., Masarie, K. A., Krol, M. C., and Peters, W.: The CarbonTracker Data Assimilation Shell (CTDAS) v1.0: implementation and global carbon balance 2001–2015, *Geosci. Model Dev.*, 10, 2785–2800, [https://doi.org/10.5194/gmd-10-](https://doi.org/10.5194/gmd-10-2785-2017) 2785-2017, 2017.
- van der Werf, G. R., Randerson, J. T., Giglio, L., van Leeuwen, T. T., Chen, Y., Rogers, B. M., Mu, M., 980 van Marle, M. J. E., Morton, D. C., Collatz, G. J., Yokelson, R. J., and Kasibhatla, P. S.: Global fire emissions estimates during 1997–2016, *Earth Syst. Sci. Data*, 9, 697–720,

<https://doi.org/10.5194/essd-9-697-2017>, 2017.

- Wang, H. M. Jiang, F., Wang, J., Ju, W. M., and Chen, J. M.: Terrestrial ecosystem carbon flux estimated using GOSAT and OCO-2 XCO₂ retrievals, *Atmos. Chem. Phys.*, 19, 12067–12082, 985 <https://doi.org/10.5194/acp-19-12067-2019>, 2019.
- Wang, J., Feng, L., Palmer, P. I., Liu, Y., Fang, S. X., Bösch, H., O'Dell, C. W., Tang, X. P., Yang, D. X., Liu, L. X., and Xia, C. Z.: Large Chinese land carbon sink estimated from atmospheric carbon dioxide data, *Nature*, 586, 720–735, <https://doi.org/10.1038/s41586-020-2849-9>, 2020.
- Wang, S. J., Kawa, R., Collatz, G. J., Sasakawa M., Gatti, L., Machida, T., Liu, Y. P., and Manyin, M. E. 990 A global synthesis inversion analysis of recent variability in CO₂ fluxes using GOSAT and in situ observations, *Atmos. Chem. Phys.*, 18, 11097–11124, <https://doi.org/10.5194/acp-18-11097-2018>, 2018.
- Wang, Y. L., Wang, X. H., Wang, K., Chevallier, F., Zhu, D., Lian, J., Yue, H., Tian, H. Q., Li, J. S., Zhu, J. X., Jeong, S. J., and Canadell, J. G.: The size of the land carbon sink in China, *Nature*, 603, 995 E7–E12, <https://doi.org/10.1038/s41586-021-04255-y>, 2022, arising from Wang et al. *Nature* <https://doi.org/10.1038/s41586-020-2849-9> (2020)
- Yang, D. X., Liu, Y., Cai, Z. N., Chen, X., Yao, L., and Lyu, D. R.: First global carbon dioxide maps produced from TanSat measurements, *Adv. Atmos. Sci.*, 35, 621–623, <https://doi.org/10.1007/s00376-018-7312-6>, 2018.
- 1000 Zhang, H. F., Chen, B. Z., van der Laan-Luijkx, I. T., Chen, J., Xu, G., Yan, J. W., Zhou, L. X., Fukuyama, Y., Tans, P. P., and Peters, W. Net terrestrial CO₂ exchange over China during 2001–2010 estimated with an ensemble data assimilation system for atmospheric CO₂, *J. Geophys. Res.-Atmos.*, 119, 3500–3515, <https://doi.org/10.1002/2013JD021297>, 2014.
- Zhang, M. G., Uno, I., Sugata, S., Wang, Z. F., Byun, D., and Akimoto, H.: Numerical study of boundary 1005 layer ozone transport and photochemical production in East Asia in the wintertime, *Geophys. Res. Lett.*, 29(11), <https://doi.org/10.1029/20001GL014368>, 2002.
- Zhang, Q. W., Li, M. Q., Wei, C., Mizzi, A. P., Huang, Y. J., and Gu, Q. R.: Assimilation of OCO-2 retrievals with WRF-Chem/DART: A case study for the Midwestern United States, *Atmos. Environ.*, 246, 118106, <https://doi.org/10.1016/j.atmosenv.2020.118106>, 2021.
- 1010 Zheng, B., Tong, D., Li, M., Liu, F., Hong, C., Geng, G., Li, H., Li, X., Peng, L., Qi, J., Yan, L., Zhang, Y., Zhao, H., Zheng, Y., He, K., and Zhang, Q.: Trends in China's anthropogenic emissions since

2010 as the consequence of clean air actions, *Atmos. Chem. Phys.*, 18, 14095–14111, <https://doi.org/10.5194/acp-18-14095-2018>, 2018.

1015 Zheng, T., French, N. H. F., and Baxter, M.: Development of the WRF-CO₂ 4D-Var assimilation system v1.0, *Geosci. Model Dev.*, 11, 1725–1752, <https://doi.org/10.5194/gmd-11-1725-2018>, 2018.

O'Dell, C. W., Eldering, A., Wennberg, P. O., Crisp, D., Gunson, M. R., Fisher, B., Frankenberg, C., Kiel, M., Lindqvist, H., Mandrake, L., Merrelli, A., Natraj, V., Nelson, R. R., Osterman, G. B., Payne, V. H., Taylor, T. E., Wunch, D., Drouin, B. J., Oyafuso, F., Chang, A., McDuffie, J., Smyth, M., Baker, D. F., Basu, S., Chevallier, F., Crowell, S. M. R., Feng, L., Palmer, P. I., Dubey, M., García, O. E., 1020 Griffith, D. W. T., Hase, F., Iraci, L. T., Kivi, R., Morino, I., Notholt, J., Ohyama, H., Petri, C., Roehl, C. M., Sha, M. K., Strong, K., Sussmann, R., Te, Y., Uchino, O., and Velazco, V. A.: Improved retrievals of carbon dioxide from Orbiting Carbon Observatory-2 with the version 8 ACOS algorithm, *Atmos. Meas. Tech.*, 11, 6539–6576, <https://doi.org/10.5194/amt-11-6539-2018>, 2018.

Wunch, D., Wennberg, P. O., Osterman, G., Fisher, B., Naylor, B., Roehl, C. M., O'Dell, C., Mandrake, 1025 L., Viatte, C., Kiel, M., Griffith, D. W. T., Deutscher, N. M., Velazco, V. A., Notholt, J., Warneke, T., Petri, C., De Maziere, M., Sha, M. K., Sussmann, R., Rettinger, M., Pollard, D., Robinson, J., Morino, I., Uchino, O., Hase, F., Blumenstock, T., Feist, D. G., Arnold, S. G., Strong, K., Mendonca, J., Kivi, R., Heikkinen, P., Iraci, L., Podolske, J., Hillyard, P. W., Kawakami, S., Dubey, M. K., Parker, H. A., Sepulveda, E., García, O. E., Te, Y., Jeseck, P., Gunson, M. R., Crisp, D., and Eldering, 1030 A.: Comparisons of the Orbiting Carbon Observatory-2 (OCO-2) XCO₂ measurements with TCCON, *Atmos. Meas. Tech.*, 10, 2209–2238, <https://doi.org/10.5194/amt-10-2209-2017>, 2017.

Figures and Tables

Captions:

1035 **Table 1.** Evaluation results between the observations and model (unit: ppm), including model results from CTRL (black, *a priori* flux simulation), FC (*italic, a posteriori* flux simulation), and AN (**bold**, analysis fields from JDAS).

Table 2. China's annual carbon sink estimated by different methods, including the inventory method, ecosystem process models, and atmospheric inversion (unit: PgC yr⁻¹).

Table 3. Probability distribution of hourly bias (unit: %) and bias standard deviation (unit: ppm) of

1040 XCO₂ validation including CTRL, FC and AN in 2016.

Table 4. Evaluation results between *in situ* observations and model, including CTRL (black, *a priori* flux simulation), FC (*italic, a posteriori* flux simulation), and AN (**bold**, analysis fields from JDAS).

Figure 1. The ensemble spread of $\lambda_{t,t}^a$ at model level 1 in January 2016, when $\beta=80$.

1045 **Figure 2.** Observation increments (XCO₂; unit: ppm) and analysis increments (biosphere flux; unit: $\mu\text{mole m}^{-2} \text{s}^{-1}$) in (a, b) January, (c, d) July, and (e, f) the whole year of 2016.

Figure 3. Horizontal distribution of CO₂ biosphere fluxes (unit: $\mu\text{mole m}^{-2} \text{s}^{-1}$): (a) E^a in 2016, the *a posteriori* fluxes; (b) $E^a - E^p$ in 2016, the differences between the *a posteriori* and *a priori* CO₂ fluxes; (c) $E^a - E^p$ in January; (d) $E^a - E^p$ in April; (e) $E^a - E^p$ in July; (f) $E^a - E^p$ in October. The red frames mark west China (28°–48°N, 85°–104°E), north China (37°–52°N, 105°–135°E), central China (30°–36°N, 105°–120°E), and south China (18°–29°N, 105°–123°E). The blue frames mark six key ecological areas of China: Daxing'anling (50°–53°N, 121°–127°E); the Loess Plateau (35°–40°N, 105°–112°E); the Qinling Mountains (32°–34°N, 104°–115°E); the rocky desert in Guangxi (22°–25°N, 106°–111°E); Mount Wuyi (26.5°–28.0°N, 117.5°–119.0°E); and Xishuangbanna (21.0°–22.6°N, 100.0°–102.0°E).

1055 **Figure 4.** Time series of CO₂ biosphere fluxes over (a) mainland China, (b) west China, (c) north China, (d) central China, and (e) south China, marked by the red frames in Fig. 3a (unit: TgC month⁻¹), in each month of 2016, obtained from *a priori* values (PR, black), *a posteriori* values (AN, red), and the flux forecast model (FC, blue). The bars on the right-hand side represent the 12-month average (unit: TgC month⁻¹). The boxes on the left-hand side denote the daily flux (unit: TgC day⁻¹), with the whiskers indicating the minimum and maximum and the horizontal lines across the box indicating the 25th percentile, the median, and the 75th percentile, respectively.

1065 **Figure 5.** Time series of CO₂ biosphere fluxes over six ecological areas of China (blue frames in Fig. 3a; unit: TgC month⁻¹), in each month of 2016, obtained from *a priori* values (PR, black bars) and *a posteriori* values (AN, red bars). The bars on the right-hand side represent the 12-month average (unit: TgC month⁻¹). The subfigures at the bottom denote the daily temperature (blue lines; unit: °C; left-hand y-axis), total solar radiation (red stars; unit: MJ d⁻¹; left-hand y-axis), and precipitation (grey bars; unit: mm d⁻¹; right-hand y-axis), with the right-hand bars representing the annual average.

Figure 6. Horizontal distribution of CO₂ biosphere fluxes averaged over each province of mainland China in 2016 (unit: $\mu\text{mole m}^{-2} \text{s}^{-1}$): (a) E^a : the *a posteriori* fluxes; (b) E^p : the *a priori* fluxes; (c)

1070 $E^a - E^p$: the differences between the *a posteriori* and *a priori* CO₂ fluxes. Note that Taiwan, Hong Kong, Macao and Shanghai are not discussed owing to the insufficient grid resolution.

Figure 7. The total *a priori* (black) and *a posteriori* (red) CO₂ biosphere fluxes over each province of mainland China in 2016 (unit: TgC yr⁻¹). The abbreviations of the provinces are: NM, Neimenggu; SC, Sichuan; GZ, Guizhou; XJ, Xinjiang; QH, Qinghai; SX, Shaanxi; GX, Guangxi; HL, Heilongjiang; GS, Gansu; SX, Shanxi; HUN, Hunan; HUB, Hubei; HEB, Hebei; NEN, Henan; JL, Jilin; XZ, Xizang; GD, Guangdong; JX, Jiangxi; CQ, Chongqing; YN, Yunnan; AH, Anhui; ZJ, Zhejiang; NX, Ningxia; BJ, Beijing; JS, Jiangsu; SH, Shanghai; FJ, Fujian; TJ, Tianjin; HAN, Hainan; LN, Liaoning; and SD, Shandong.

Figure 8. The annual-averaged horizontal distribution of CO₂ concentrations (unit: ppm) near the surface in 2016: (a) AN: the analysis concentration; (b) FC-AN: the difference between the *a posteriori* flux simulation and analysis concentration fields; (c) CTRL-AN: the difference between the *a priori* flux simulation and analysis concentration fields; (d) the XCO₂ error reduction [see text for calculation; blue, with the standard deviation (\pm) of the analysis XCO₂ provided] and independent XCO₂ data amount (black stars, rescaled to 1:10) over 8°–57°N and 105°–120°E at different latitudes.

1085

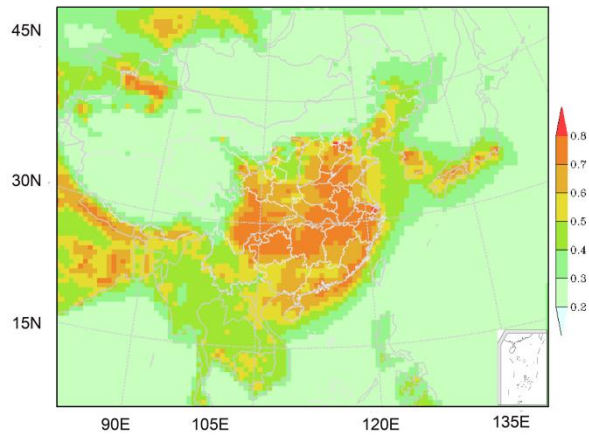
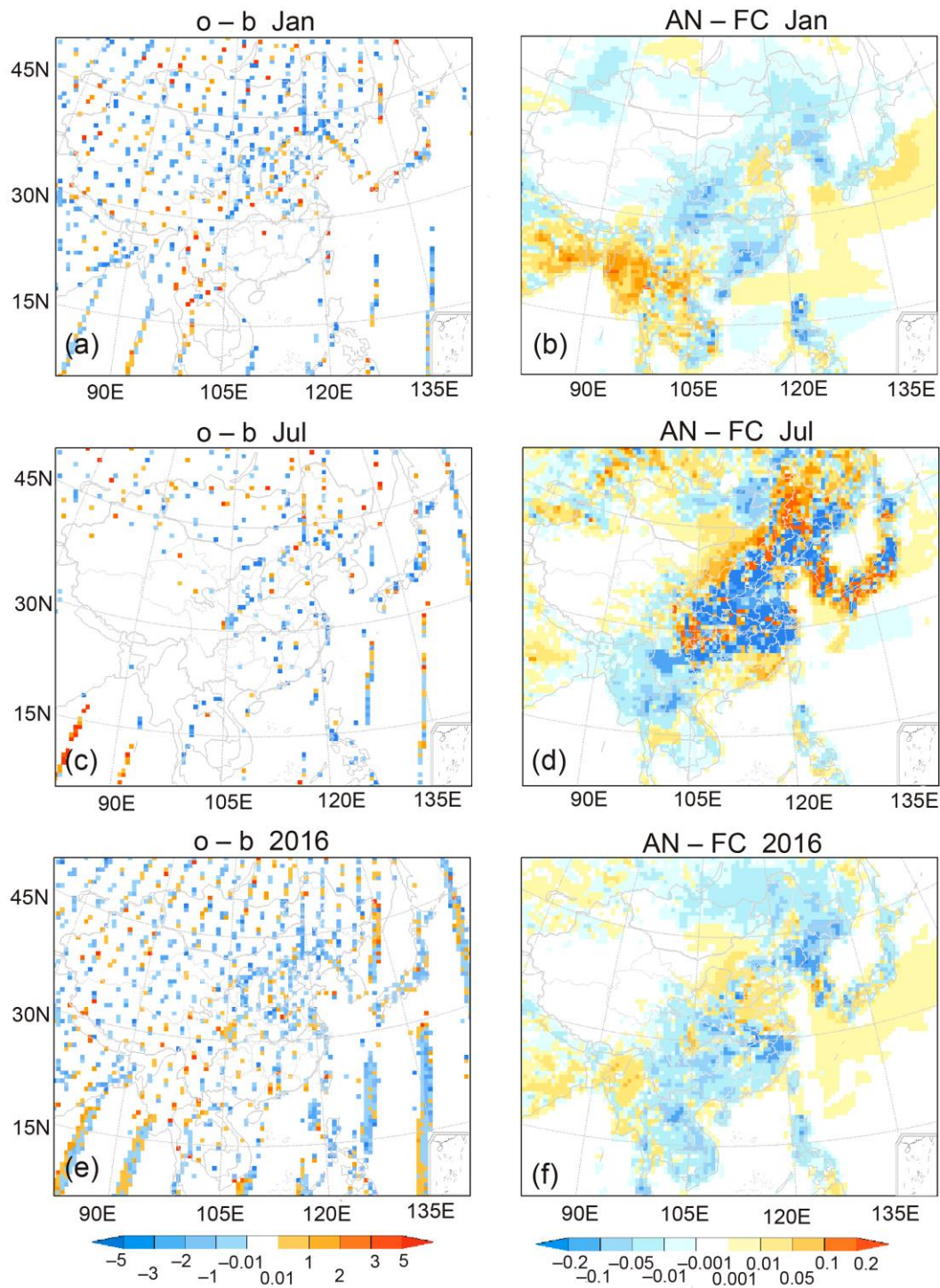


Figure 1. The ensemble spread of $\lambda_{i,t}^a$ at model level 1 in January 2016, when $\beta=80$.



1090 **Figure 2.** Observation increments (XCO₂; unit: ppm) and analysis increments (biosphere flux; unit: μmole m⁻² s⁻¹) in (a, b) January, (c, d) July, and (e, f) the whole year of 2016.

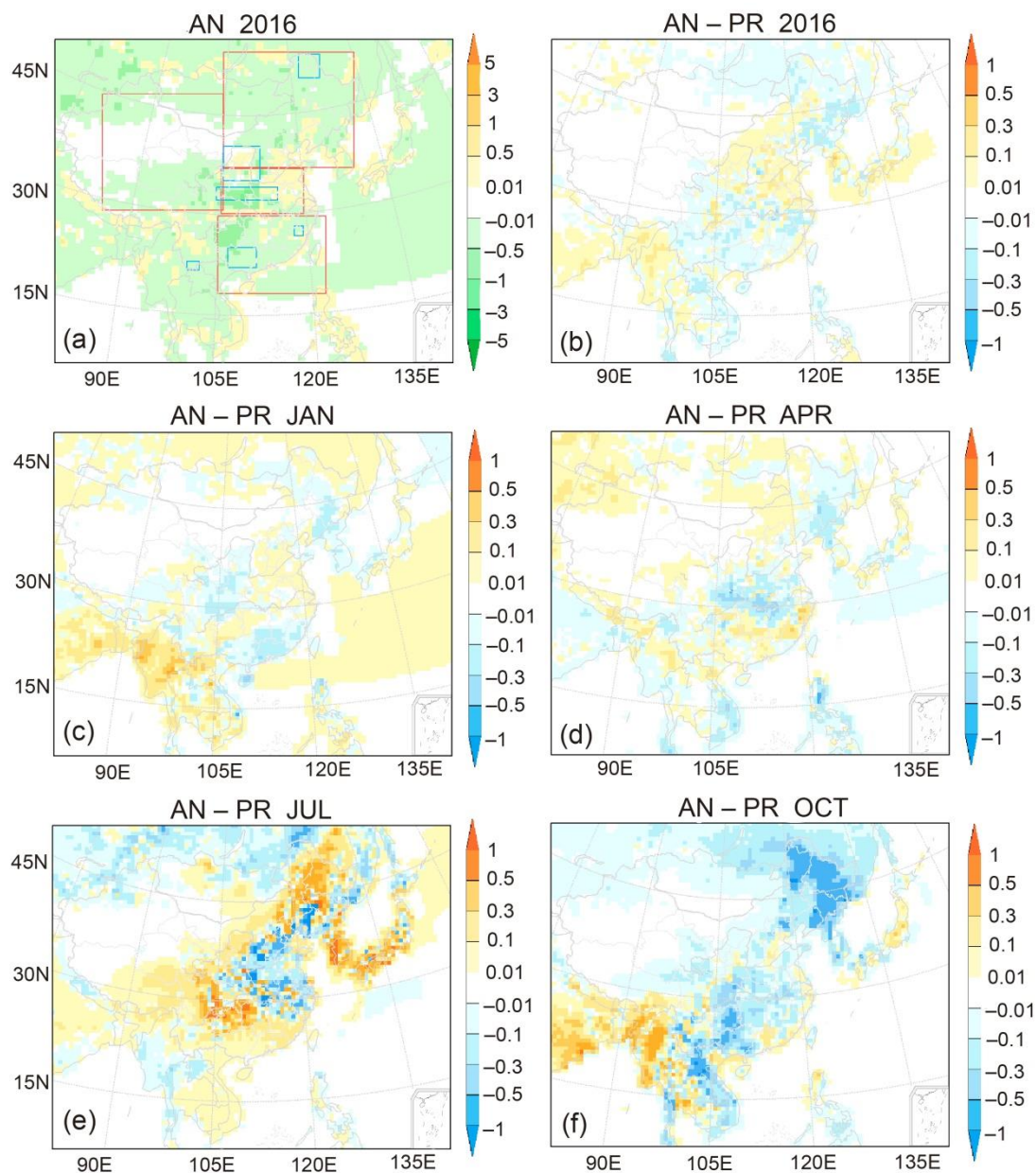


Figure 3. Horizontal distribution of CO₂ biosphere fluxes (unit: $\mu\text{mole m}^{-2} \text{s}^{-1}$): (a) E^a in 2016, the *a posteriori* fluxes; (b) $E^a - E^p$ in 2016, the differences between the *a posteriori* and *a priori* CO₂ fluxes; (c) $E^a - E^p$ in January; (d) $E^a - E^p$ in April; (e) $E^a - E^p$ in July; (f) $E^a - E^p$ in October. The red frames mark west China (28°–48°N, 85°–104°E), north China (37°–52°N, 105°–135°E), central China (30°–36°N, 105°–120°E), and south China (18°–29°N, 105°–123°E). The blue frames mark six key ecological areas of China: Daxing'anling (50°–53°N, 121°–127°E); the Loess Plateau (35°–40°N, 105°–112°E); the Qinling Mountains (32°–34°N, 104°–115°E); the rocky desert in Guangxi (22°–25°N, 106°–111°E); Mount Wuyi (26.5°–28.0°N, 117.5°–119.0°E); and Xishuangbanna (21.0°–22.6°N, 100.0°–102.0°E).

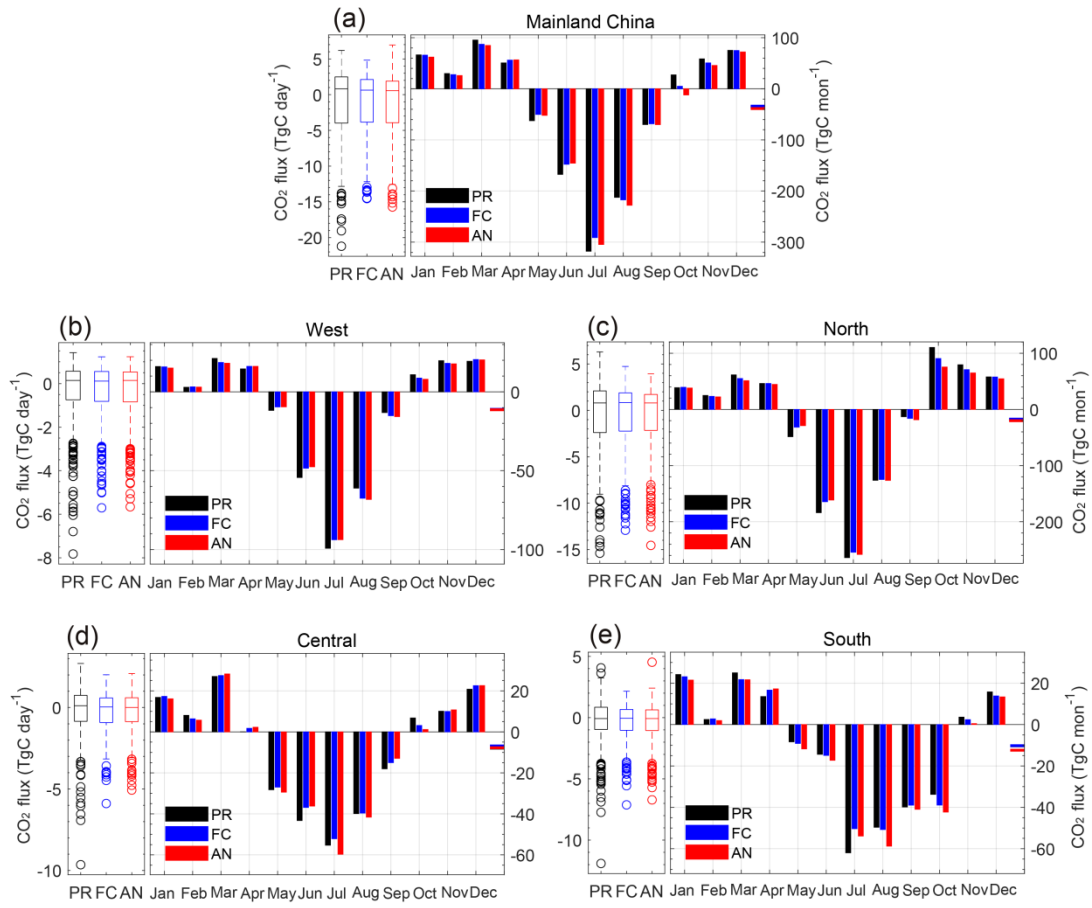
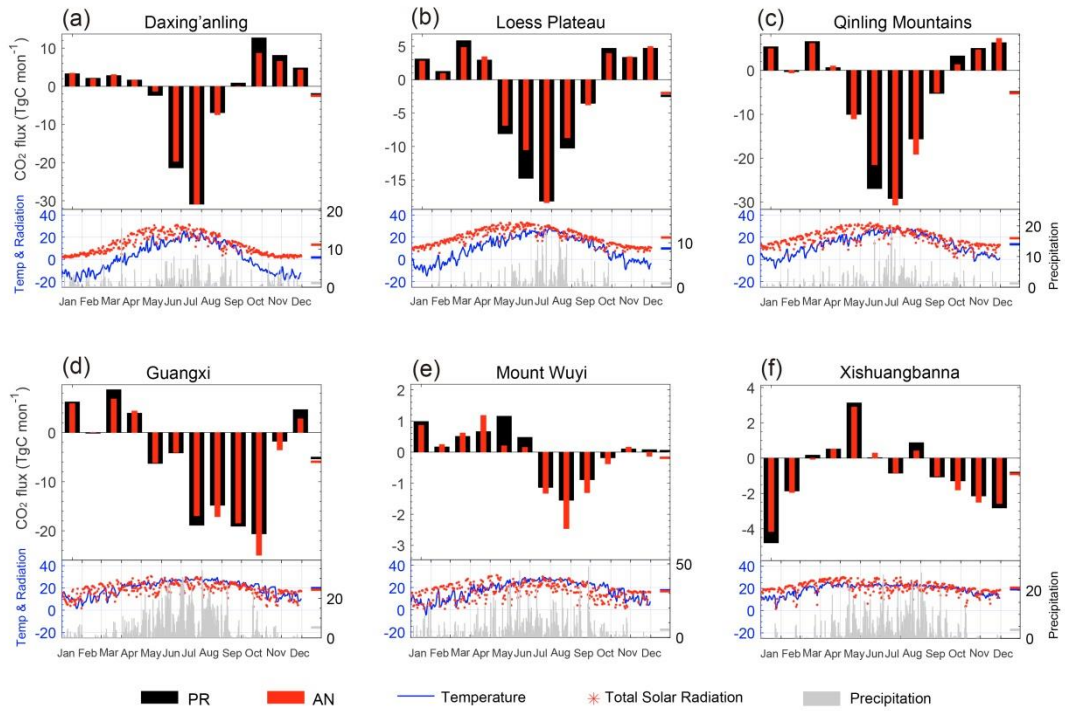


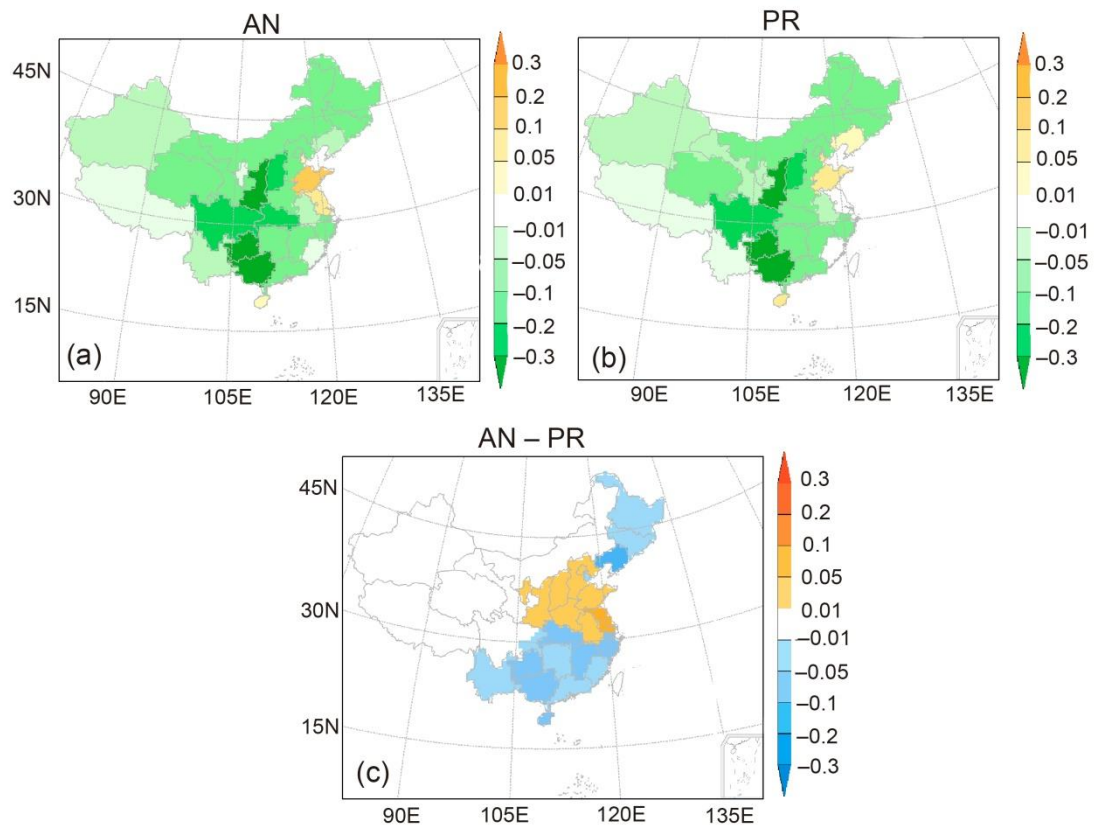
Figure 4. Time series of CO₂ biosphere fluxes over (a) mainland China, (b) west China, (c) north China, (d) central China, and (e) south China, marked by the red frames in Fig. 3a (unit: TgC month⁻¹), in each month of 2016, obtained from *a priori* values (PR, black), *a posteriori* values (AN, red), and the flux forecast model (FC, blue). The bars on the right-hand side represent the 12-month average (unit: TgC month⁻¹). The boxes on the left-hand side denote the daily flux (unit: TgC day⁻¹), with the whiskers indicating the minimum and maximum and the horizontal lines across the box indicating the 25th percentile, the median, and the 75th percentile, respectively.

1105

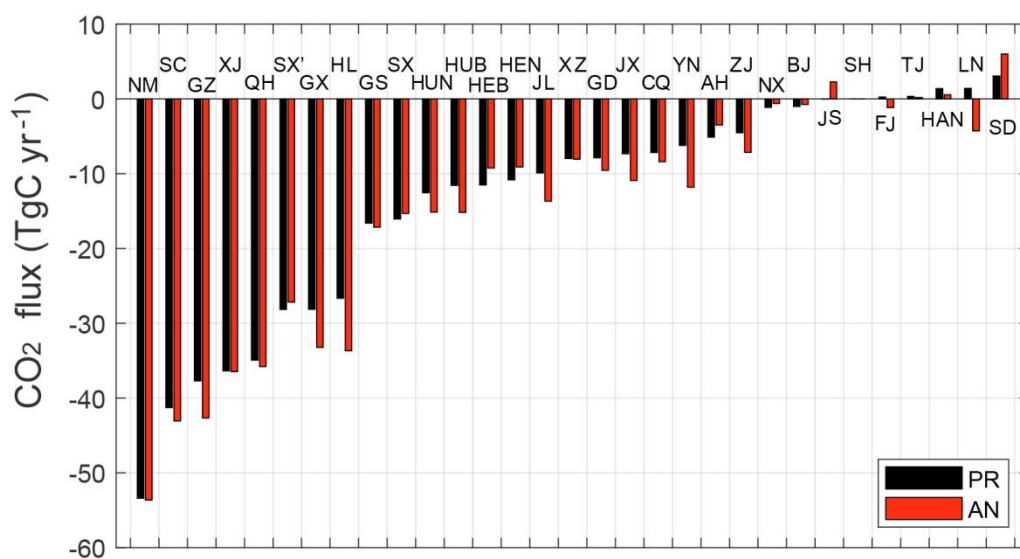
1110



1115 **Figure 5.** Time series of CO₂ biosphere fluxes over six ecological areas of China (blue frames in Fig. 3a; unit: TgC month⁻¹), in each month of 2016, obtained from *a priori* values (PR, black bars) and *a posteriori* values (AN, red bars). The bars on the right-hand side represent the 12-month average (unit: TgC month⁻¹). The subfigures at the bottom denote the daily temperature (blue lines; unit: °C; left-hand y-axis), total solar radiation (red stars; unit: MJ d⁻¹; left-hand y-axis), and precipitation (grey bars; unit: mm d⁻¹; right-hand y-axis), with the right-hand bars representing the annual average.



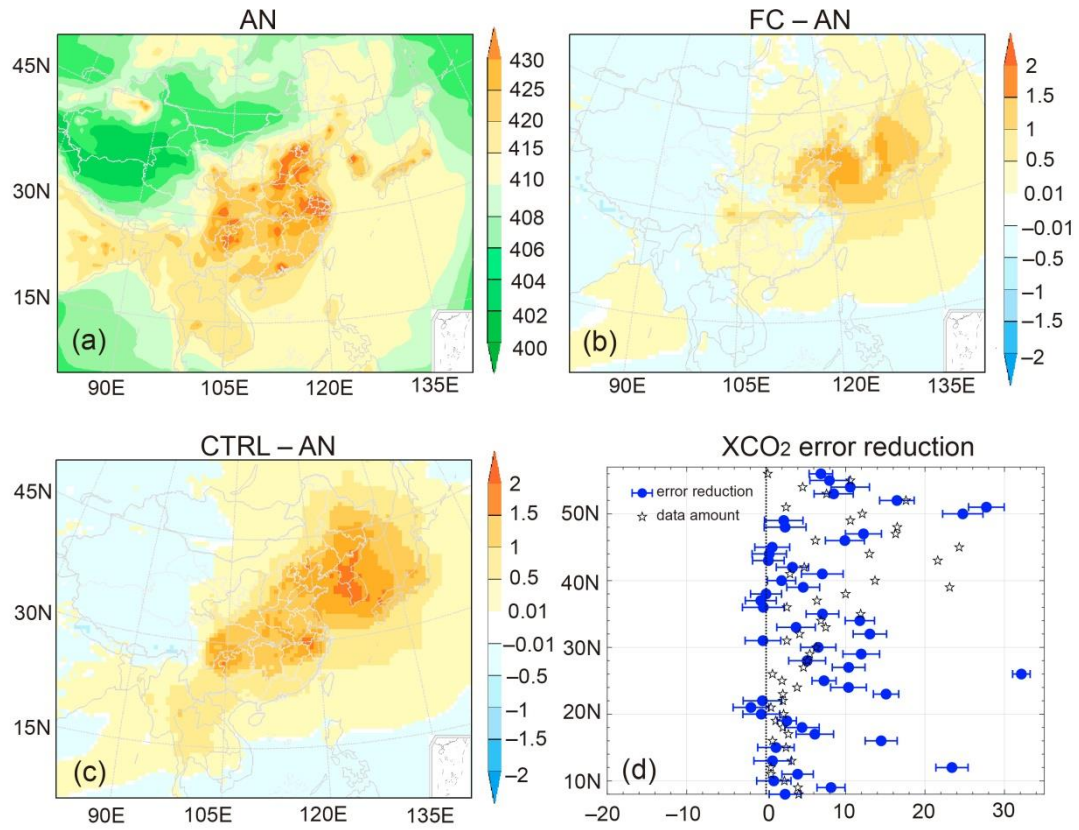
1120 **Figure 6.** Horizontal distribution of CO₂ biosphere fluxes averaged over each province of mainland China in 2016 (unit: $\mu\text{mole m}^{-2} \text{s}^{-1}$): (a) E^a : the *a posteriori* fluxes; (b) E^p : the *a priori* fluxes; (c) $E^a - E^p$: the differences between the *a posteriori* and *a priori* CO₂ fluxes. Note that Taiwan, Hong Kong, Macao and Shanghai are not discussed owing to the insufficient grid resolution.



1125

Figure 7. The total *a priori* (black) and *a posteriori* (red) CO₂ biosphere fluxes over each province of mainland China in 2016 (unit: TgC yr⁻¹). The abbreviations of the provinces are: NM, Neimenggu; SC, Sichuan; GZ, Guizhou; XJ, Xinjiang; QH, Qinghai; SX', Shaanxi; GX, Guangxi; HL, Heilongjiang; GS, Gansu; SX, Shanxi; HUN, Hunan; HUB, Hubei; HEB, Hebei; HEN, Henan; JL, Jilin; XZ, Xizang; GD, Guangdong; JX, Jiangxi; CQ, Chongqing; YN, Yunnan; AH, Anhui; ZJ, Zhejiang; NX, Ningxia; BJ, Beijing; JS, Jiangsu; SH, Shanghai; FJ, Fujian; TJ, Tianjin; HAN, Hainan; LN, Liaoning; and SD, Shandong.

1130



1135 **Figure 8.** The annual-averaged horizontal distribution of CO₂ concentrations (unit: ppm) near the surface
 1140 in 2016: (a) AN: the analysis concentration; (b) FC-AN: the difference between the *a posteriori* flux
 simulation and analysis concentration fields; (c) CTRL-AN: the difference between the *a priori* flux
 simulation and analysis concentration fields; (d) the XCO₂ error reduction [see text for calculation; blue,
 with the standard deviation (\pm) of the analysis XCO₂ provided] and independent XCO₂ data amount
 (black stars, rescaled to 1:10) over 8°–57°N and 105°–120°E at different latitudes.

Table 1. Evaluation results between the observations and model (unit: ppm), including model results from CTRL (black, *a priori* flux simulation), FC (*italic, a posteriori* flux simulation), and AN (**bold**, analysis fields from JDAS).

		XCO ₂ (assimilation)				XCO ₂ (validation)			
	NUM	RMSE (BG)	CORR (BG)	MAE (BG)	Median of XCO ₂ uncertainty	RMSE (CTRL/FC/AN)	CORR (CTRL/FC/AN)	MAE (CTRL/FC/AN)	NUM
Jan	1788	2.38	0.53	1.97	0.66	3.80/3.79/ 2.45	0.19/0.19/ 0.46	2.45/2.45/ 2.05	2024
Feb	1870	2.29	0.52	1.87	0.72	2.42/2.40/ 2.37	0.42/0.42/ 0.43	1.99/1.98/ 1.97	1902
Mar	1617	2.26	0.49	1.83	0.78	2.48/2.46/ 2.40	0.36/0.37/ 0.38	2.05/2.03/ 2.00	1409
Apr	1346	2.18	0.36	1.76	0.91	1.90/1.90/ 1.79	0.31/0.32/ 0.35	1.91/1.91/ 1.84	1037
May	1090	2.36	0.16	1.95	0.91	2.70/2.71/ 2.47	0.18/0.18/ 0.17	2.23/2.23/ 2.10	826
Jun	734	2.21	0.72	1.78	0.97	2.34/2.35/ 2.26	0.70/0.70/ 0.73	1.84/1.83/ 1.82	615
Jul	728	2.41	0.80	1.99	0.99	2.45/2.44/ 2.37	0.82/0.82/ 0.83	2.02/2.02/ 1.98	560
Aug	842	2.38	0.69	1.98	0.95	2.49/2.50/ 2.42	0.65/0.65/ 0.66	2.03/2.03/ 2.01	742
Sep	854	2.15	0.47	1.76	0.82	2.26/2.22/ 2.11	0.37/0.38/ 0.43	1.82/1.80/ 1.71	879
Oct	1190	2.29	0.45	1.88	0.75	2.37/2.28/ 2.22	0.37/0.40/ 0.44	1.91/1.86/ 1.84	1192
Nov	1517	2.27	0.60	1.85	0.67	2.39/2.36/ 2.25	0.54/0.55/ 0.58	1.91/1.89/ 1.84	1627
Dec	1688	2.26	0.60	1.85	0.64	2.36/2.35/ 2.34	0.52/0.52/ 0.53	1.94/1.93/ 1.91	1847
2016	15264	2.29	0.72	1.87	0.77	2.65/2.63/ 2.34	0.66/0.66/ 0.73	2.03/2.02/ 1.93	14660

1145 Note. “XCO₂ (validation)” denotes the independent GOSAT XCO₂ retrievals for validation. “XCO₂ (assimilation)” represents the observations used for assimilation, and the corresponding model results come from BG (JDAS background fields). RMSE refers to the root-mean-square error; CORR refers to the correlation coefficient; MAE refers to the mean absolute bias; and NUM refers to the XCO₂ data amount. The monthly and annual averages were calculated from the hourly outputs.

1150

Table 2. China’s annual carbon sink estimated by different methods, including the inventory method, ecosystem process models, and atmospheric inversion (unit: PgC yr⁻¹).

Method	Carbon sink	Period covered					Reference
Inventory	-0.18± 0.07	1980–1999					Piao et al., 2009
	-0.29± 0.12	2000–2009					Jiang et al., 2016
	-0.28	2009–2018					Wang et al., 2022
Ecosystem process models	-0.17± 0.04	1980–2002					Piao et al., 2009
	-0.18	1961–2005					Tian et al., 2011
	-0.12±0.08	1982–2010					He et al., 2019
Inversion		Observations	Transport models	Optimization	Resolution		
<i>CAMS</i>	-0.35± 0.033	1996–2005	<i>in situ</i> CO ₂	<i>LMDZ</i>	<i>Bayesian</i>	3.75°×2.5°, monthly	<i>Piao et al., 2009</i>
<i>CAMS-v19</i>	-0.25	2010–2016	<i>in situ</i> CO ₂	<i>LMDZ</i>	<i>Variational</i>	3.75°×1.875°, 8 days,	<i>Wang et al., 2022</i>
<i>BI</i>	-0.51 ± 0.18	2006–2009	<i>in situ</i> CO ₂	<i>TM5</i>	<i>Bayesian</i>	3°×2°, weekly	<i>Jiang et al., 2016</i>
<i>CT-China</i>	-0.39 ± 0.33	2006–2009	<i>in situ</i> CO ₂	<i>TM5</i>	<i>EnSRF</i>	1°×1°, weekly	<i>Jiang et al., 2016</i>
CT-China	-0.33	2001–2010	<i>in situ</i> CO ₂	TM5	EnSRF	1°×1°, weekly	Zhang et al., 2014
CT-China	-0.27±0.20	2010	<i>in situ</i> CO ₂	TM5	EnSRF	1°×1°, weekly	Chen et al., 2021
CT-China	-0.41±0.22	2010–2012	GOSAT XCO ₂	TM5	EnSRF	1°×1°, weekly	Chen et al., 2021
CT-Europe	-0.32	2010-2015	<i>in situ</i> CO ₂	TM5	EnSRF	1°×1°, weekly	van der Laan-Luijkx et al., 2017
UoE	-1.11 ± 0.38	2010–2016	<i>in situ</i> CO ₂	GEOS-Chem	EnKF	4°×5°, 8 days	Wang et al., 2020
UoE	-0.83 ± 0.47	2010–2015	GOSAT XCO ₂	GEOS-Chem	EnKF	4°×5°, 8 days	Wang et al., 2020
UoE	-0.68	2015	OCO-2 XCO ₂	GEOS-Chem	EnKF	2°×2.5°, 8 days	Schuh et al., 2022
JCS	-0.48	2010-2015	<i>in situ</i> CO ₂	TM3	Bayesian	4°×5°, monthly	Rödenbeck et al., 2018
GCASv2	-0.34 ± 0.14	2010–2015	GOSAT XCO ₂	MOZART-4	EnSRF	1°×1°, weekly	He et al., 2022
CCDAS	-0.43 ± 0.09	2010–2015	<i>in situ</i> CO ₂ , FAPAR	TM2	4D-Var	2°×2°, monthly	He et al., 2022
CT-2019B	-0.43	2016	<i>in situ</i> CO ₂	TM5	EnSRF	1°×1°, weekly	Jacobson et al., 2020
JDAS	-0.68	2016	<i>in situ</i> CO ₂	CMAQ	EnKS	64×64km, hourly	Peng, et al., 2023
JDAS	-0.47	2016	GOSAT XCO ₂	CMAQ	EnKS	64×64km, hourly	This study

Note. *Italic* font and gray shading denote the inversion results after correcting for lateral fluxes according to the flux gap between top-down and bottom-up estimation. The abbreviations used in the table are as follows: CAMS, Copernicus Atmosphere Monitoring Service; BI, Bayesian Inversion; JCS, Jena CarboScope; CCDAS, Carbon Cycle Data Assimilation System; FAPAR, remotely sensed Fraction of Absorbed Photosynthetically Active Radiation; LMDZ, Laboratoire de Météorologie Dynamique Zoom, a global transport model; and TM5, the global atmospheric Tracer Model 5.

Table 3. Probability distribution of hourly bias (unit: %) and bias standard deviation (unit: ppm) of XCO₂ validation including CTRL, FC and AN in 2016.

Bias probability distribution	CTRL	FC	AN
[-4,4]	89.64	89.89	91.02
[-3,3]	75.63	75.99	76.84
[-2,2]	56.13	56.45	56.88
[-1,1]	30.22	30.08	30.24
[0,4]	53.43	53.62	55.74
[0,3]	44.65	44.86	46.21
[0,2]	32.26	32.46	33.07
Bias standard deviation	2.6268	2.6072	2.2674

1165 **Table 4.** Evaluation results between *in situ* observations and model, including CTRL (black, *a priori* flux simulation), FC (*italic, a posteriori* flux simulation), and AN (**bold**, analysis fields from JDAS).

	Lat.(°N) /Lon.(°E)	OBS. NUM	OBS. Freq.	RMSE (CTRL/FC/AN)	RMSE Imp. Rate FC/AN (%)	MAE (CTRL/FC/AN)	MAE Imp. Rate FC/AN (%)	General Site Description
Longfengshan	44.73/127.60	840	Hourly	10.94/10.87/ 10.38	0.63/ 5.16	7.83/7.81/ 7.72	0.30/ 1.40	Forest (Northeast China)
Shangdianzi	40.65/117.12	1620	Hourly	10.00/9.87/ 9.74	1.34/ 2.58	6.87/6.62/ 6.64	3.53/ 3.26	Cropland (North China)
Mt. Waliguan	36.28/100.90	338	Daily	7.05/6.64/ 6.31	5.78/ 10.43	4.63/4.38/ 4.15	5.35/ 10.35	Tibet Plateau (China)
Shangri-La	28.00/99.40	1709	Hourly	9.76/9.62/ 9.44	1.42/ 3.21	7.21/7.08/ 7.02	1.72/ 2.61	Forest (Southeast China)
Lin'an	30.30/119.72	1410	Hourly	9.42/9.49/ 8.60	-0.73/ 8.70	6.63/6.78/ 6.14	-2.16/ 7.45	Forest (East China)
Jinsha	29.63/114.22	30	Weekly	9.21/9.41/ 8.94	-2.13/ 2.96	6.96/7.04/ 6.46	-1.15/ 7.13	Urban (Central China)
King's Park	22.31/114.17	364	Daily	22.12/21.63/ 21.10	2.22/ 4.63	17.02/16.68/ 16.06	1.98/ 5.06	Urban (Hong Kong, China)
Ulaan Uul	44.45/111.08	49	Weekly	5.50/5.41/ 5.22	1.62/ 5.06	3.70/3.63/ 3.52	2.02/ 5.09	Grassland (Mongolia)
Ryori	39.03/141.82	8553	Hourly	6.85/6.77/ 6.06	1.08/ 11.51	4.59/4.48/ 3.91	2.21/ 14.68	Mountain (Japan)
Mt. Dodaira	36.00/139.20	7928	Hourly	7.62/7.51/ 7.12	1.45/ 6.50	5.37/5.31/ 5.00	1.22/ 6.95	Mountain (Japan)
Kisai	36.08/139.55	8686	Hourly	17.09/15.90/ 15.80	6.99/ 7.56	13.00/12.22/ 12.24	5.99/ 5.83	Urban (Japan)
Anmyeon-do	36.53/126.32	3228	Hourly	16.00/14.03/ 13.81	12.34/ 13.70	10.42/9.41/ 8.85	9.73/ 15.06	Coastal (Korea)
Jeju Gosan	33.30/126.21	4373	Hourly	10.10/9.85/ 8.79	2.42/ 12.97	7.29/7.12/ 6.34	2.39/ 13.10	Ocean (Korea)
Yonagunijima	24.47/123.02	8085	Hourly	9.24/9.21/ 8.60	0.25/ 6.86	7.39/7.38/ 6.91	0.08/ 6.41	Ocean (Japan)
AVE				10.78/10.44/ 9.99	2.48/ 7.27	7.78/7.57/ 7.21	2.37/ 7.49	

Note. 'Lat./Lon.' refers to the latitude and longitude of site; 'OBS. NUM' refers to the observation amount; 'OBS. Freq.' refers to the observation time frequency; 'RMSE Imp. Rate' refers to the improvement rate of RMSE, i.e., $(RMSE_{CTRL}-RMSE_{FC})/RMSE_{CTRL}\times 100\%$ and $(RMSE_{CTRL}-RMSE_{AN})/RMSE_{CTRL}\times 100\%$; 'MAE Imp. Rate' refers to the improvement rate of MAE, i.e., $(MAE_{CTRL}-MAE_{FC})/MAE_{CTRL}\times 100\%$ and $(MAE_{CTRL}-MAE_{AN})/MAE_{CTRL}\times 100\%$, respectively. The annual averages were calculated from the hourly output.

1170